Role of fluid on earthquake occurrence: Example of the 2019 Ridgecrest and the 1997, 2009 and 2016 Central Apennines sequences

Jugurtha Kariche[1,2]

[1] USTHB, Laboratoire de Géophysique, FSTGAT, Algiers, Algeria.

[2] Institut Terre et Environnement de Strasbourg (ITES), CNRS-UMR7063.

[*]Corresponding author: Jugurtha Kariche (jugurtha.kariche@usthb.edu.dz or jkariche@gmail.com)

ABSTRACT

This paper focuses on the study of the temporal evolution of seismicity and the role of fluids during major earthquake sequences that occurred in the Central Apennines and Southern Walker Lane belt-Eastern California Shear Zone over the last two decades: The 1997 Colfiorito, the 2009 L'Aquila, the 2016 Amatrice-Norcia, and the 2019 Ridgecrest sequences. The availability of high-quality earthquakes catalogs offers the opportunity to evaluate in detail the temporal evolution of the earthquake's size distribution (or b-value) and propose a physical explanation based on the effect of the fluid flow process in triggering seismicity. For all seismic sequences, the b-value time series show a gradual decrease from a few months to one year before mainshocks. The gradual decrease in the b-value is interpreted as a gradual increase in earthquake activity due essentially to the short-term to intermediate-term pore-fluid fluctuations. The temporal variation of the b-value during Amatrice-Norcia and Ridgecrest foreshock sequences is characterized by a double b-value minimum separated by a short-lived b-value increase as observed in laboratory experiments on water-saturated rocks. The observed fluctuation of the b-value is presented here as an accelerating crack growth due essentially to the fluid flow instability. Even though seismic precursors could have been predictable in areas with high dense seismic networks, the different b-value time series reveal the difficulty in establishing a correspondence between the duration of the foreshock activity and the magnitude of the next largest expected earthquake. This may suggest that the fluid migration controls the size of the ruptures.

Key words: Seismicity and tectonics; Fractures, faults, Fluids; Neotectonics

INTRODUCTION

Several studies have suggested a relation between the occurrence of earthquake sequences and the temporal change in the relative size distribution of earthquakes quantified by the Gutenberg-Richter (GR) b-value (Berg, 1968; Scholz, 1968; Smith, 1981; Wiemer & Wyss, 2000 among others). The analyses of a series of 60 foreshocks and 428 aftershocks related to three moderate earthquakes occurring in the Fairbanks region of Alaska show that the Gutenberg-Richter (GR) b-value was abnormally low (between 0.34 to 0.45) before large events and was restored taking a typical value of 0.85 to 0.95 during and after each mainshock (Berg, 1968). The seismicity analysis of the 1967 Caracas (Mw 6.7) earthquake sequence, the 1971 San Fernando (Mw 6.4) earthquake sequence, and the 1968–1978 New Zealand earthquake sequence reveals that the temporal variation in the b-value was remarkably coupled with the size of moderate to strong earthquakes (Berg, 1968). A large time scale decrease in the b-value associated with an acceleration of aseismic slip is observed before the Mw 8.1 Iquique, Chile, and the Mw 9.0 Tohoku-Oki earthquakes (Nanjo et al., 2012; Scholz, 2019). Several studies argue that the acceleration of aseismic slip is favored by variation of pore fluid pressure at depth (Segall & Rice, 1995; Ruhl et al., 2016;Cappa et al., 2019 ; De Barros et al., 2020). The gradual decrease in the b-value on a much shorter time scale is also observed in the four-month-long foreshock sequence preceding the 2009 L'Aquila earthquake (Gulia et al., 2016). The temporal variation of the b-value before the L'Aquila mainshock correlates with the change of Vp/Vs from January to April 6 (Lucente et al., 2010). The simultaneous change in b-value and Vp/Vs in the case of the L'Aquila sequence may be interpreted as a nucleation process due to an overpressurized volume controlled by fluid migration at depth (Chiaraluce, 2012).

The comparison between the temporal evolution of b-value and the effective normal stress in California shows a decrease in the b-value associated with a decrease in the effective normal stress rate (Khoshmanesh & Shirzaei,2018). The maximum increase in the Coulomb stress rate

(up to 0.45 bar/yr spanning the period from 2003 to 2010) along the central part of the San Andreas Fault system also coincides with the decrease in effective normal stress caused by the evolution of pore-fluid pressure at depth (Khoshmanesh & Shirzaei, 2018). These results argue that a strong correlation exists between the fluid migration and the temporal evolution of the b-value along the central part of the San Andreas Fault. In the Southern Walker Lane belt (SWL)–Eastern California Shear Zone (ECSZ), high-resolution optical satellite imagery analysis reveals a considerable contribution of the inelastic processes to the total diffuse deformation following the 2019 Ridgecrest earthquake sequence (Antoine et al., 2021). The high Vp/Vs ratio covering the complex fault zones of the 2019 Ridgecrest foreshock–mainshock sequence (Tong et al., 2021) denotes that the change in the pore-fluid pressure near the Ridgecrest fault zone may be considered as one of the plausible mechanisms explaining the diffuse inelastic deformation observed during the 2019 Ridgecrest sequence. A stress change modeling result taking into account the variation in the Vp/Vs ratio due to the diffusive effect of fluids during the Mw 6.4 Ridgecrest foreshock indicates that the value of fluid diffusivity necessary to trigger the next Mw 7.1 mainshock is estimated to be $\leq 2.32 \times 10^4$ cm^2/s (Kariche, 2022).

A laboratory fracturing experiment on fluid-saturated rocks predicts a variation in the Vp/Vs due to the change in the rheological properties of the seismogenic crust following large earthquakes. Fracture mechanics modeling and laboratory experiments for dry and water-saturated specimens show that the gradual decrease in the b-value related to a progressive increase in acoustic emission rate (AE) is only visible in water-saturated rocks (Main et al., 1990). Laboratory experiments at constant pore-fluid volume also predict a fluctuation in the b-value before major cracks and support the idea that the fluid considerably affects the size and the distribution of future cracks (Sammonds et al., 1992). Other correlations between b-value and fluid migration are also found in the crustal range of the Taiwan orogenic belt (Chen et al., 2019). Although these studies have demonstrated a connection between the variation in the b-

value and the influence of fluids, none have successfully proposed a unified physical mechanism that explains the occurrence of seismic sequences, the stress evolution, and the effect of fluids across different phases related to the generation of earthquake sequences.

In this paper, I explore the influence of fluid migration on earthquake occurrence by analyzing the temporal evolution of seismicity for two tectonically active zones with available high-quality, dense seismic networks: the Central Apennines (Italy) and the SWL–ECSZ (CA). Several major seismic sequences are studied in detail: the 1997 Colfiorito, the 2009 L'Aquila, and the 2016 Amatrice–Norcia for the Central Apennines seismic zone, and the 2019 Ridgecrest sequence for the SWL–ECSZ. These sequences are explored in terms of seismic productivity and related fluid migration. By analyzing the evolution of seismicity and stress redistribution, I found a causative relation between the pore-fluid effect and the spatiotemporal evolution of crack growth before and during earthquakes. The results are also compared to the laboratory experiments for a better constraint on the role of fluids in the different phases of earthquake generation. Based on these findings, I propose a physical mechanism that connects pore-fluid effects and stress redistribution in controlling the earthquake preparation process, including the behavior of foreshock evolution. Using the poromechanical analysis as presented in this paper, I further explore the influence of b-value changes on earthquake forecasting. Additionally, considering poroelastic stress change modeling results and the analysis of postseismic deformation processes, the influence of fluids on the occurrence of aftershock sequences is also debated.

SEISMOTECTONICS SETTING, FLUID FLOW AND MECHANICAL PROPERTIES OF FAULT ZONES

1. THE CENTRAL APENNINE SEQUENCE

The 1997, 2009, and 2016 Central Apennines earthquake sequences start with the 1997 Colfiorito (Umbria–Marche) sequence, which struck the northern part of the Apennines in Italy (Amato *et al.*, 1998; Stramondo *et al.*, 1999; Deschamps *et al.*, 2000; Chiaraluce *et al.*, 2003). The Colfiorito sequence is characterized by six earthquakes with a magnitude larger than 5.0 and two earthquakes with a magnitude larger than 5.7 (Figure 1, Figure 2A & S1). The first earthquake occurred on September 26 at 00:33 UTC with a magnitude Mw = 5.7 (Ekström *et al.*, 1998). Nine hours later, another strong earthquake with Mw 6.0 struck the Colfiorito region at 3 km from the first event (Figure 1). The Mw 5.7 and Mw 6.0 events were preceded by a series of foreshocks that began on September 3, occurring in the area between the epicenters of the two main events (Ripepe *et al.,* 2000). The hypocentral depths of the Mw 5.7 and Mw 6.0 events are approximately equal and situated at 5.04 and 4.95 km depth, respectively (Figure S1). The third event with a magnitude Mw = 5.9 triggers 18 days after at 12 km southeast of the first event (Figure S1). The analysis of the spatial and temporal evolution of seismicity related to the 1997 Colfiorito sequence shows that the seismicity is mainly controlled by the poroelastic properties of the seismogenic zone and the fluid flow process (Antonioli *et al.* 2005). Using the fluid triggering hypothesis, the value of fluid diffusivity associated with the triggering process of the 1997 Colfiorito sequence is estimated to range between 2.2×10^5 and 9.0×10^5 cm^2/s (Antonioli *et al.,* 2005).

On April 6, 2009, at 01:32 GMT, a devastating earthquake with a magnitude Mw 6.3 occurred on a normal fault at the intramontane basin near the city of L'Aquila (Lucente *et al.*, 2010; Figure 1). This sequence began with a series of foreshocks six months prior to the mainshock in a ~4 km long band on the L'Aquila fault zone (Figure 2B; Figures S3A and C). The near-field seismic wave analysis shows that the spatiotemporal evolution of foreshocks correlates with a clear variation in seismic wave properties at depth (Lucente *et al.,* 2010). The Vp/Vs value rose from 1.85 to more than 1.92 near the epicenter area of the 2009 L'Aquila

158 earthquake a week before the mainshock, and decreased to 1.85 a few hours before (Lucente et
159 al., 2010). The change in Vp/Vs near L'Aquila is interpreted as the variation in elastic properties
160 of the medium due to the fluid migration along the L'Aquila fault zone (Lucente *et al.,* 2010;
161 Chiaraluce, 2012; Scholz, 2019). Based on the temporal change in the Vp/Vs ratio, the
162 triggering mechanism related to the L'Aquila earthquake is resolved as a mechanism governed
163 by the presence of a deep, large fluid reservoir (Lucente *et al.,* 2010). Indeed, the complexity
164 of the fault zone, the deep thrust fault, and the low-angle active normal faults observed near the
165 L'Aquila major rupture (Chiodini *et al.*, 2004) may be interpreted as a structural seal that favors
166 the fluid accumulation and creates an overpressurized volume near the L'Aquila hypocentral
167 depth.

168 From the structural point of view, the evolution of fault geometry near the L'Aquila fault
169 zone seems to be controlled by a set of conjugate EW–NS fault systems in a transtensional
170 regime at the limit of large active fault segments. The aftershock distribution analysis following
171 the 2009 L'Aquila mainshock indicates that a significant portion of the aftershock productivity
172 (~32% of the total aftershocks recorded during the period from April to December 2009) is
173 concentrated at the limit of the fault slip zone. Seismological investigations and pore-fluid
174 pressure modeling results suggest that the spatiotemporal evolution of aftershocks at the limit
175 of the L'Aquila fault was primarily driven by a reduction in fault strength of 7–10 MPa, largely
176 attributed to the fluid-flow processes (Malagnini *et al*., 2012).

177 After the 2009 L'Aquila earthquake, the Central Apennine was followed by three moderate
178 earthquakes with a magnitude $M \geq 6.0$: the 2016 August 24 Amatrice earthquake (Mw 6.2), the
179 2016 August 26 Ussita (Visso) earthquake (Mw 6.1), and the 2016 October 30 Norcia
180 earthquake (Mw 6.5) (Figure 1). Thus, this sequence fills the gap between the Colfiorito and
181 L'Aquila earthquake series (Figure 1). The focal mechanism of the three earthquakes shows a
182 normal faulting solution (Figure 1) consistent with the active extension rate of 3–4 mm/yr in

183 the Apennines zones revealed by GPS (Serpelloni *et al.*, 2005). The mechanics of deformation
184 in the Central Apennines are complex. The strain release near the Amatrice fault zone is
185 accommodated by a complex interaction between the main normal faults and secondary
186 structures inherited from the pre-Quaternary compressional tectonic phases (Cheloni *et*
187 *al.*,2017).
188 The spatiotemporal analysis of seismicity between the Amatrice and Visso earthquakes predicts
189 a fluid diffusivity value of 1.5 m^2/s, corresponding to a northward migration rate of 0.4 km/day
190 (Pino et al., 2019; Tung & Masterlark, 2018). However, the fluid diffusivity along individual
191 fault branches within the 2016 Amatrice–Norcia earthquake sequence reveals a range of fluid
192 diffusivity between 50 and 2000 m^2/s (Malagnini *et al*., 2022). The differences in fluid
193 characteristics reported by various authors (Antonioli *et al.*, 2005; Tung & Masterlack, 2018;
194 Pino *et al.* 2019; Malagnini *et al.,* 2022) correlate with the variation in seismicity from south to
195 north in the Apennine fault zone (Figure 1). This variation in fluid diffusivity may explain the
196 high degree of heterogeneity along the Apennines fault zone and the differences in the time
197 characteristics between major earthquakes.

198

199

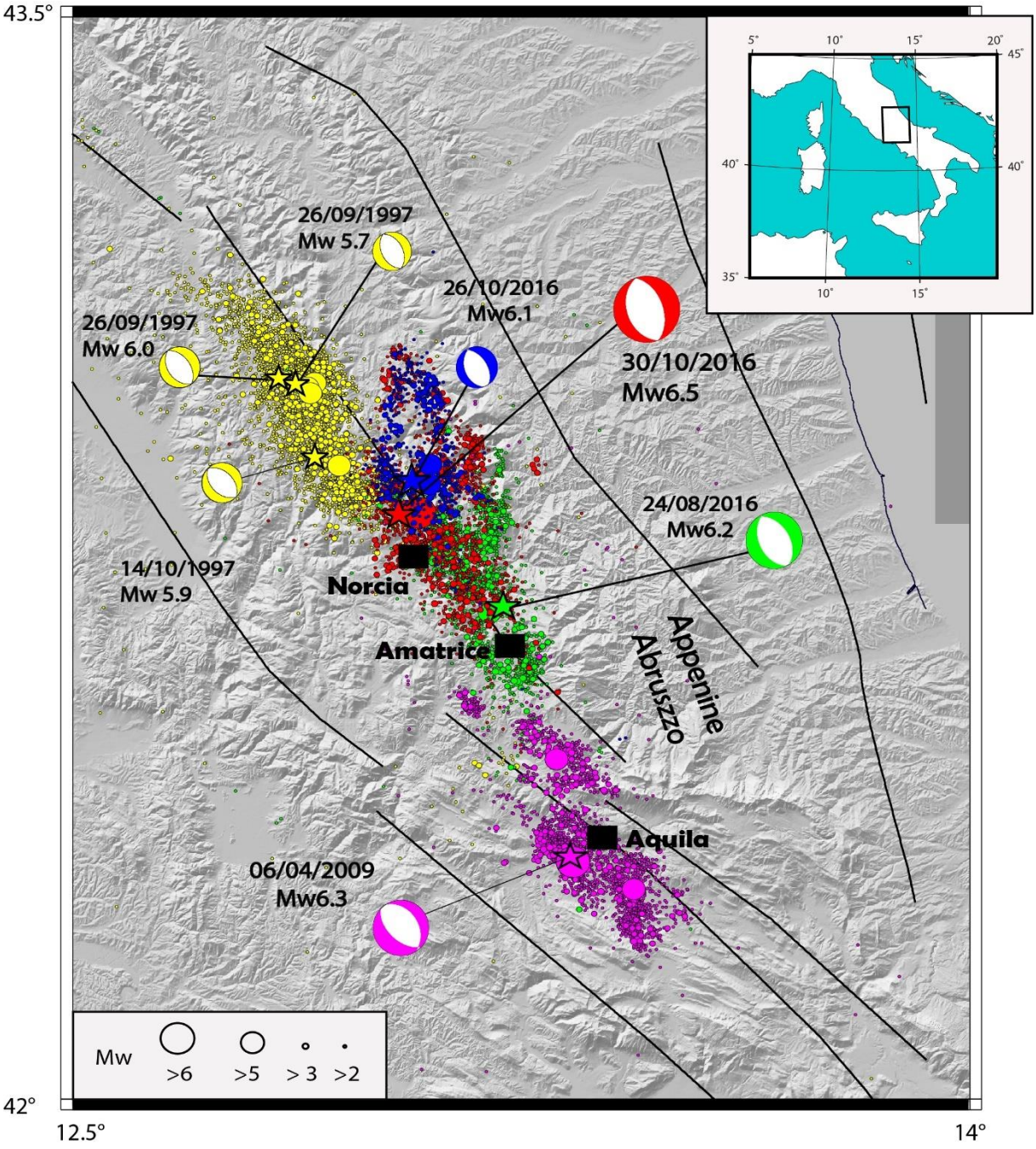

Figure 1: *Seismicity and focal mechanisms of major earthquakes occurred in the central Apennines (Italy) spanning the period from 1997 to 2016. Each earthquake sequence with a related mainshock focal mechanism is represented by specified color. For example, the magenta color represents the spatial distribution of the events associated with the 2009 L'Aquila earthquake sequence, the focal mechanism associated to the L'Aquila mainshock is also represented by the same color. The focal solutions are from the Global Centroid Moment*

Tensor (https://www.globalcmt.org/). The seismicity of the Central Apennine is from INGV (https://doi.org/10.13127/ISIDE). The inset figure represents the location of the studied area. Note that the 2016 Amatrice-Norcia seismic sequence may view as a unique earthquake swarm divided into three smaller sequences. The colored data (green, blue, red) mimic the seismic migration from the August 24th (sequence in green), and culminating with the October 30th, Mw 6.5 earthquake (sequence in red).

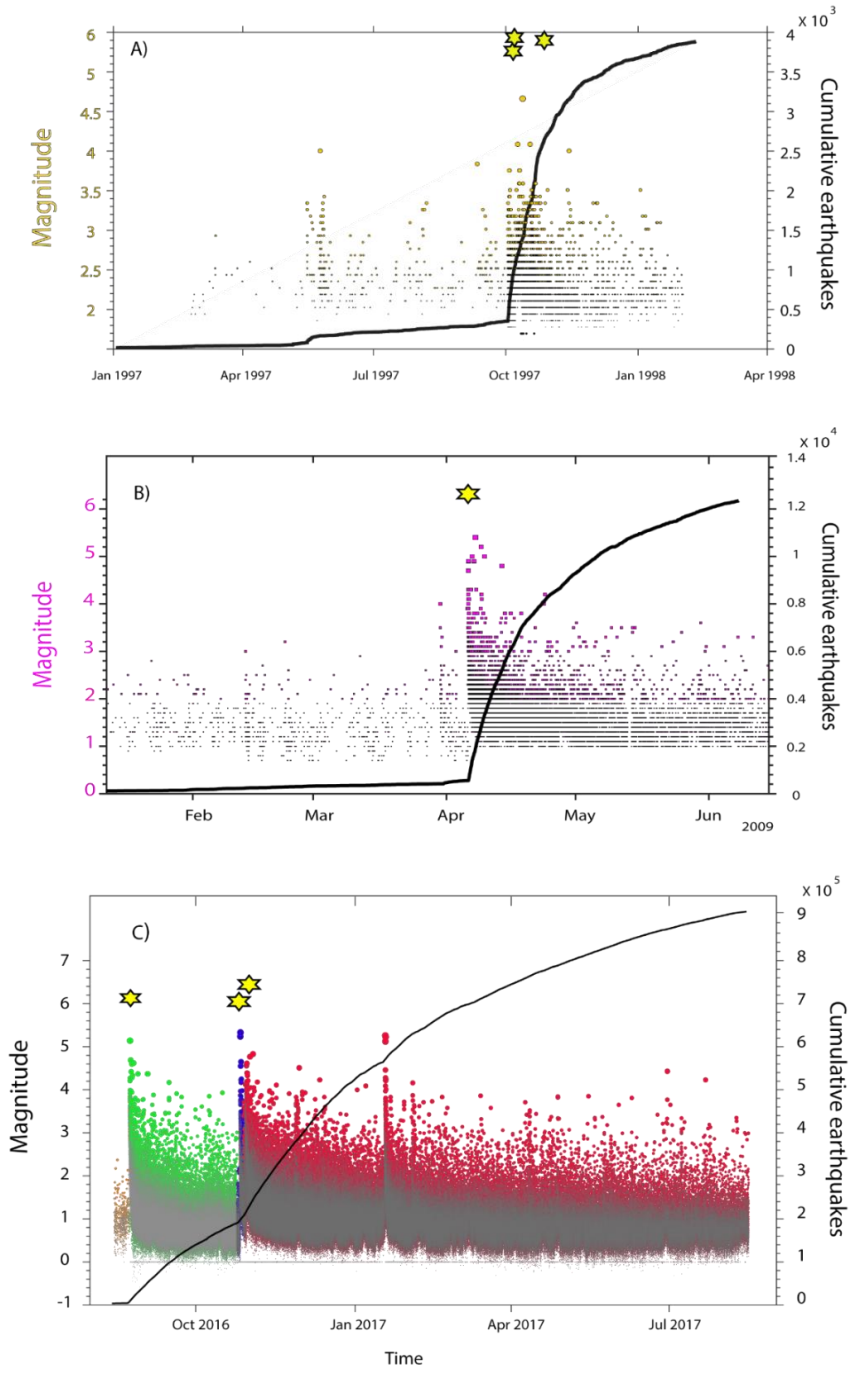

Figure 2: *Evolution of the Cumulative number of earthquakes and magnitude distribution through time for:* ***A)*** *the 1997 Colfiorito sequence,* ***B)*** *the 2009 L'Aquila sequence and* ***C)*** *the 2016 Amatrice-Norcia sequence. The earthquakes datasets used for A) and B) are from INGV (https://doi.org/10.13127/ISIDE). The earthquake database used for construct the C) plot is derived from a high precise determination of ~900, 000 earthquakes derived from deep-neural-network-based picker (Tan et a.,2021). The earthquake magnitude evolution in time from each sequence is represented by a specific color same as in Figure 1. The yellow stars represent the major events for each sequence. The Time evolution of earthquakes and related magnitude distribution are constructed using the Zmap software (Wyss & Wiemer.,2000).*

2. THE 2019 RIDGECREST SEQUENCE

In July 2019, two moderate to strong earthquakes with a magnitude Mw 6.4 and 7.1 struck Ridgecrest (California) in the SWL–ECSZ region (Fielding *et al.,* 2020). Earthquake rupture characteristics deduced from Interferometric Synthetic Aperture Radar (InSAR), source time functions, and early aftershock analysis indicate that the Mw 6.4 and the Mw 7.1 earthquakes occurred on strike-slip faults within a time interval approximately equal to 34 hours at 12 km distance and ranging depth of 4 to 8 km (Figure 3; Barnhart *et al*., 2019; Fielding *et al.,* 2020, Toda & Stein, 2020). Early surface deformation analysis deduced from InSAR and focal mechanism analysis indicate that the 2019-07-04 (Mw 6.4) and the 2019-07-06 (Mw 7.1) events occurred on NE–SW and NW–SE trending conjugate strike-slip faults. The Ridgecrest fault zone is a part of the Indian Wells Valley, which is connected to the Central Basin and Range tectonic province. This area is bounded on the west by the Sierra Nevada Mountains, on the south by the Garlock fault, and on the east by the Walker Lane belt (Figure 3). The Little Lake (or Ridgecrest) fault zone (LLFZ) is defined as an important component of the SWL–ECSZ which accommodates a non-negligible part of the Pacific–North America plate boundary displacement (Figure 3). The seismotectonics of the Ridgecrest region reflect the complex

interaction of left-lateral and right-lateral strike-slip faults in a variable tectonic regime (Figure 3). The transition from transpressional regimes near LLFZ to transtensional regimes north of Ridgecrest (near Coso Range) agrees with the rotation of the maximum principal stress (Combs 1980). This may be interpreted as a consequence of a significant weakening mechanism affecting immature faults. In this context, pressurized fluids trapped within heterogeneous and complex fault zones experience dynamic changes in fluid flow processes. These changes tend to reduce effective normal stress and, consequently, influence the strength of the faults during the early stages of fault-rupture growth.

Based on the poromechanical model proposed by Rice (1992), Axen (1992) interprets the active deformation along the low-angle normal fault in the Indian Wells Valley–Coso Range as a consequence of a weakening mechanism due to abnormally elevated pore-fluid pressure in both brittle and ductile regimes. In this case, the permeability in the active fault zone must be higher than its surrounding rocks. Large volumes of fluid migrating from ductile to brittle zone in active mylonite areas are also observed in relation to the detachment zones in the Central Mojave Desert (Axen, 1992). The analysis of high-resolution imaging derived from satellite optical imagery shows that the presence of inelastic failure related to the 2019 Ridgecrest earthquake sequence reflects a mylonitic deformation of the fault damage zone (Barnhart *et al*., 2020). The observed mylonitic zones are directly correlated to the degree of fault maturity of the Ridgecrest conjugated ruptures. The analysis of Line-of-Sight (LOS) Interferometric Synthetic Aperture Radar (SAR) displacements following the 2019 Ridgecrest sequence attests that a part of the observed early 2019 Ridgecrest postseismic deformation is indicative of a poroelastic rebound (Wang & Bürgmann, 2020). The LOS displacements derived from both Sentinel-1 and COSMO-SkyMed (CSK) SAR data reveal that the maximum postseismic deformation along the LOS of ascending satellite tracks is located northwest of the Mw 7.1 epicenter near the Coso geothermal fault zone (Wang & Bürgmann, 2020).

Most of the seismicity recorded before the 2019 Ridgecrest sequence is relatively small (M ≤ 3). The largest event recorded in SWL is the 1872 M7.5 Owens Valley earthquake (Figure S2; Monastero *et al.,* 2002). The 1872 M7.5 Owens Valley earthquake is dominated by a right-lateral shearing deformation along the Owens Valley fault (Figure S2). The recurrence of earthquakes with a magnitude M ≥ 5.0 in SWL is approximately equal to 20 years, with two significant sequences with four moderate events (M ≥ 5.0) that occurred near Ridgecrest between 1995 and 1998 (Hauksson *et al.,* 1995). This recurrence pattern has culminated in the occurrence of the 2019 Ridgecrest sequence (Mw 6.4; Mw 7.1). The study of the mechanics of earthquake and fault interaction in the context of conjugate strike-slip faults indicates a clear influence of fluid migration on the occurrence of moderate to large earthquakes in the SWL tectonic domain (Kariche, 2022). Based on the Coulomb poroelastic stress change modeling approach, the time delay between two conjugate strike-slip earthquakes seems to be coupled to the variation in fluid diffusivity along heterogeneous faults (Kariche, 2022). These observations are in concordance with the Cocco & Rice (2002) Coulomb stress transfer modeling results taking into account the presence of high pore-fluid pressure at hypocentral depth.

Considering the ~34 hr characteristic time representing the time delay between the Mw 6.4 and the Mw 7.1 events (Kariche, 2022) and a fluid viscosity of 3×10^{-4} Pa·s, the average value of permeability necessary to trigger the Mw 7.1 Ridgecrest event is estimated between 10^{-14}–10^{-15} m². Despite the fact that this value is higher than the value obtained by Cocco and Rice (2002) for normal fault geometries, it seems to be in good agreement with the permeability values obtained by Miller (2020) for the 1992 Landers–Big Bear conjugated sequence and based entirely on the conceptual model of permeability dynamics as proposed by the same author. Additionally, this estimation of permeability aligns well with the value obtained by Nespoli *et al.* (2018) for the 2012 Emilia–Romagna earthquake sequence. The temporal and spatial evolution of major events following the Mw 6.4 foreshock sequence may explain the

significant increase in the value of permeability along cracks following the Mw 7.1 event. Based on this assumption, the temporal distribution of earthquake frequency and related moment release must predict a temporal fluctuation of the G–R b-value during the 2019 Ridgecrest sequence caused essentially by the variation of pore-fluid pressure at depth.

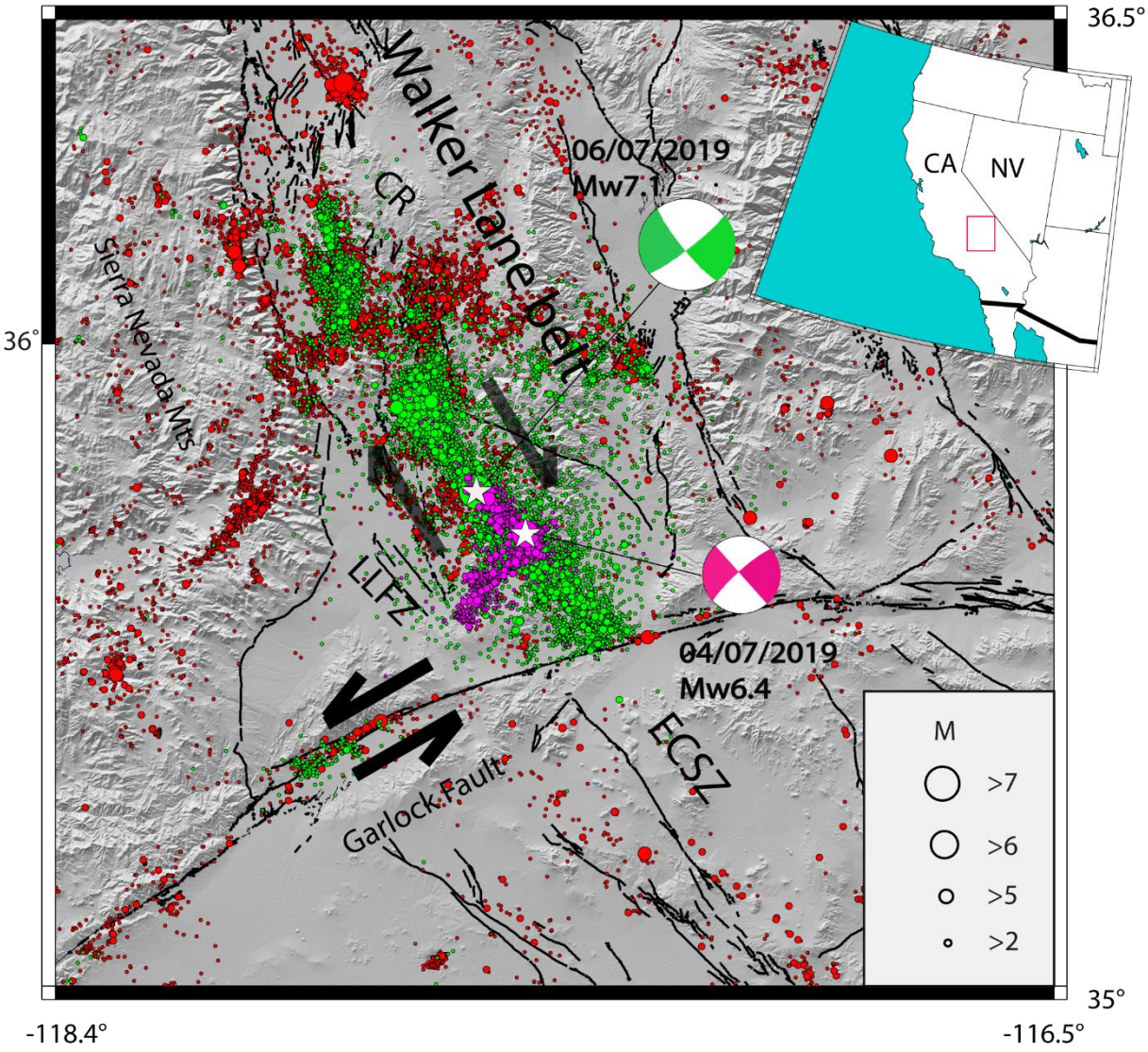

Figure 3: *Seismicity along the Southern Walker Lane (SWL)-Eastern California Shear zone (ECSZ) from 2008 to 27/10/2019 using combined SCEDC QTM catalog (Ross et al. 2019) and the high definition NEIC-USGS catalog. The color circles indicate the seismicity at different periods: red from the period between 1980 and July 2019; magenta for the period covering the 2019 Ridgecrest foreshock activity and green for events following the Mw7.1 mainshock.*

The stars show the location of the (Mw 6.4) and the 06/07/2019 (Mw 7.1) earthquakes. The red rectangle in the inset figure represents the studied area. LLFZ= Little Lake Fault Zone. CR= Coso Range. CA=California State. NV= Nevada State.

METHODOLOGY AND DATA

It's widely recognized that elevated fluid pressure exerts a crucial role in earthquake-triggering mechanics by reducing the frictional strength of the fault (Hickman *et al*., 1995; Sibson, 2000; Yamashita & Tsutsumi, 2018a; Kariche *et al*., 2018). The fluid-flow process can also play a fundamental role during earthquake sequences by encouraging the production of aftershocks (Nur & Booker, 1972; Malagnini *et al*., 2012; Kariche *et al*., 2018; Chiarabba *et al*., 2020). To quantify the influence of fluids in the nucleation, growth, and development of large-scale earthquakes and related aftershock sequences, I use several techniques based on both earthquake statistics and physics. The first step consists of developing a conceptual model based on the joint analysis of the temporal evolution of the earthquake frequency–magnitude distribution and pore-fluid flow before and during the Ridgecrest and Central Apennines sequences. The analysis is also constrained by poroelastic stress change modeling scenarios and previous laboratory results on fractured rocks (e.g., Sammonds *et al*., 1992) in order to give a robust estimation of the role of fluids on earthquake generation. The second step is to investigate a physics-based model of aftershock occurrence on the basis of the assumption that the production of aftershocks is intimately linked to the fluid-flow diffusion process. As for the first step, the analysis of the influence of the fluids on aftershock generation is also aided by poroelastic stress change modeling results taking into account both undrained and drained fluid phases.

1. G-R b-value time series modeling

A first empirical relation between the frequencies and magnitudes of earthquakes is proposed by Gutenberg & Richter (1950):

$$Log_{10}[N(M)] = a - bM \qquad (1)$$

Where a and b are the G-R constants, M is the magnitude, and $N(M)$ is the number of earthquakes in a specific time window of events with a magnitude range between M and $\pm \delta M$.

The b-value for an entire catalog is given by the maximum likelihood estimation (Aki, 1965):

$$b = \frac{1}{ln(10)(\bar{M} - M_c)} \qquad (2)$$

Where $\overline{M}$ represents an average magnitude value for a population of earthquakes satisfying the condition $M \geq M_c$, and M_c is the magnitude of completeness defined as the lowest magnitude at which all the events in a space-time volume are detected (Wiemer & Wyss, 2000; Woessner & Wiemer, 2005).

The b-value time series can be rewritten as (Woessner & Wiemer, 2005):

$$b = \frac{Log_{10}(e)}{\left[\langle M \rangle - \left(M_c - {}^{\Delta M_{bin}}/_{2}\right)\right]} \qquad (3)$$

Where $\langle M \rangle$ represents the mean magnitude of the sample and ΔM_{bin} is the binning width of the catalogue (Aki, 1965).

The standard deviation of b-value can be obtained using the Shi & Bolt (1982) approach:

$$\delta b = 2.3\, b^2 \sqrt{\frac{\sum_i (M_i - \{M\})}{n\,(n-1)}}$$

Where n is the sample size. The term $\sum_i (M_i - \{M\})$ is related to the distribution function of the mean magnitude where $\{M\}$ define the mean magnitude.

Earthquake Data and Completeness

In order to evaluate the temporal variation of seismicity on a seismogenic volume, the variation in b-value is computed using the 3D frequency–magnitude approach (Wyss *et al.,* 1998) with an appropriate time window. The procedure adopted here consists of varying the time-length windows to provide a robust estimation of the b-value at each point in time. The b-value time series computation procedure used in this study is, in general, similar to those used by Gulia & Wiemer (2019) or Dascher-Cousineau *et al*. (2020), which take into account the space–time evolution of Mc in the b-value estimation. The determination of Mc is based on the assumption that the seismic events are self-similar (Wiemer & Wyss, 2000). The most robust way to deal with the dependence of the b-value time series on Mc is to choose a large value of Mc for the entire time series catalog, but this approach leads to maximizing uncertainties when the computation of the b-value is made for a smaller number of earthquake samples.

The completeness magnitude (Mc) for each earthquake sample is assessed using an automated procedure that accounts for its temporal variability, based on the Maximum Curvature (MAXC) method (Wiemer & Wyss, 2000), Mc and the corresponding b-value are estimated simultaneously by identifying the maximum of the first derivative of the frequency–magnitude distribution. In regions with dense seismic networks and access to high-quality catalogs, the MAXC technique enables a reliable time-resolved estimation of b-values. It also reduces uncertainties associated with smaller sample sizes, which often affect fixed-Mc approaches. The latter may obscure short-term b-value variations due to over-smoothing.

To mitigate the known underestimation of Mc by the MAXC method, a correction factor of +0.2 to +0.5 is systematically added (Table 1). This adjustment accounts for the observation that the overall shape of the b-value time series remains robust across a range of reasonable Mc values specific to each earthquake sequence.

For periods with limited instrumental coverage, particularly in the Italian earthquake catalog between 1998 and 2005, when Mc may remain elevated over extended intervals, a fixed Mc approach is preferred (Table 1). This method reduces bias in b-value estimation and avoids artificial inflation of b-values caused by unrecognized drops in Mc due to undetected small-magnitude events. By applying a uniform magnitude threshold across all time windows, including those affected by seismic gaps, the fixed Mc approach ensures greater consistency than MAXC in this context. This, in turn, enhances the interpretability of b-value temporal trends, as Mc becomes decoupled from fluctuations in catalog completeness. Conversely, for events occurring after 16 April 2005, when higher-resolution data are available, the MAXC method is preferred.

Earthquake Sequence	**Time Period**	**Mc Values**	**Methodology / Notes**
2019 Ridgecrest	Before Mw 6.4	0.84 – 1.4	Estimated using MAXC method, corrected by +0.2 – 0.5 for stability Final consistent Mc ≈ 1.4 used for robust time series. Temporal b-value estimates remain stable within Mc ∈ [1.1, 2.0] via Lilliefors test
	Between Mw 6.4 and Mw 7.1	0.66 – 1.2	
	After Mw 7.1	0.4 – 1.2	
2016 Amatrice-Norcia	Full Seq	0.9– 2.3	Estimated using MAXC method, corrected by +0.2 – 0.5 for stability, results validated via bootstrapping Temporal b-value estimates remain stable within Mc ∈ [2.1, 2.5] via Lilliefors test
2009 L'Aquila	Foreshock Seq	1.4	MAXC method with a correction factor of +0.2 aligned with Gulia et al. (2016) predictive approach MAXC method consistent with a Fixed Mc
1997 Colfiorito	Full Seq	2.5	Fixed Mc with δMc = 0.1–0.2; used for stable estimates; comparable with variable-Mc result trends.

Table1: Summary of Mc values and technics used in b-value time series computation.

For the 2019 Ridgecrest sequence, I use the high-confidence Quake Template Matching (QTM) seismicity catalog for Southern California (Ross *et al.,* 2019), which spans the period from 2000 to 2018, along with the USGS-NEIC updated high-resolution catalog from March 2018 to March 2020, and the higher-resolution dataset from Shelly (2020) focused on the Ridgecrest aftershock sequence. For the 1997, 2009, and 2016 Central Apennines sequences, I rely on the complete seismic catalog of the Istituto Nazionale di Geofisica e Vulcanologia (INGV), covering the period from 1985 to 2018 (https://doi.org/10.13127/ISIDE), in combination with the regional catalog by Gasperini *et al.* (2013), augmented by the high-resolution catalog from Tan et al. (2021) for the 2016–2017 Amatrice–Norcia sequence. Duplicate events resulting from the combination of multiple catalogs are automatically identified and removed using the ZMAP software (Wiemer, 2001). A space–time window algorithm (e.g. Gardner & Knopoff, 1974) is applied to flag similar events occurring within defined proximity in both space and time. The catalogs are then merged into a single file, with redundant events eliminated accordingly. For more details on magnitude homogenization and catalog processing, refer to the "EARTHQUAKE MAGNITUDE" section in the Supplementary Material.

To investigate in detail the role of fluids before and after major earthquakes, I compare the temporal evolution of the b-value in the Central Apennines with that observed following the 2019 Ridgecrest sequence (Table 1). The b-value time series method involves analyzing the frequency–magnitude distribution over sliding time windows of fixed event counts. This approach allows more accurate estimation of b-value changes over time, improving our ability to constrain seismicity evolution across periods of highly variable seismic rates (Tormann *et al.*, 2013). Assuming that the b-value time series reflects the temporal evolution of crack density or stress heterogeneity in a seismogenic zone, the Mc threshold for each time window is selected in accordance with the magnitude distribution. b-values are computed using the maximum

likelihood method (Wyss & Wiemer, 2000), and temporal variations in Mc are incorporated in the analysis following each mainshock to minimize the influence of completeness bias on the resulting b-value time series.

The Ridgecrest zone is divided into 0.15° x 0.15° grids. The computation is made regarding the approach based on a fixed number of events of 250 with a 50 minimum event higher than the local value of Mc by using the MAXC method with magnitude binning equal to 0.1. Considering the change in the Mc value, I obtain an Mc value range of [0.84, 1.4] before the Mw 6.4 event and [0.66, 1.2] from the period between the Mw6.4 and Mw7.1 Ridgecrest mainshocks. After the Mw7.1 event, the Mc value range between [0.4, 1.2] (see Table 1). In order to reduce uncertainties on the b-values estimations, and as mentioned before, I asses Mc using the maximum curvature approach and I add 0.2-0.5 to the value of Mc. I confirm that the value of Mc that gives a reasonable estimate of the temporal evolution of the b-value is about 1.4 (Figures S5, S7; S8). Furthermore, using the Lilliefors test for statistical validation, I confirm that b-value estimates remain stable within a completeness magnitude range of **[1.1, 2.0]** (Table 1; see also the "ANALYSIS AND ROBUSTNESS OF THE B-VALUE AND MC" section in the Supplementary Material). A similar methodology was applied to the Central Apennines earthquake sequences (Table 1). In these cases, the MAXC technique also produced reliable time-resolved b-value estimates while reducing uncertainty due to small sample sizes, especially when compared to other estimation methods (Figures S4, S6, S9, S10).

Multiple b-value time series tests were performed using varying event counts, ranging from 50 to 500 events per window (Figures S11, S12). These variations allowed for an effective balance between signal resolution and smoothing. The earthquake occurrence time was used to define the temporal windows, which yielded a sampling interval of approximately 1 to 12 months, depending on the window size. Importantly, the overall shape of the b-value time series remained stable for $100 \leq N \leq 500$ in both the 2016 Amatrice–Norcia and 2019 Ridgecrest

426 sequences (Figures S11, S12). These findings are consistent with earlier studies, such as Wyss
427 & McNutt, (1998) in their analysis of the 1989 earthquake swarm beneath Mammoth Mountain
428 (CA) and Tormann *et al* (2013) who modeled temporal correlations between b-value changes
429 and surface creep in the Parkfield (California) region.

430 **2. Fluid flow and the evolution of seismicity**

431 Taking into account the complexity of earthquake generation, a realistic representation of
432 the temporal evolution of seismicity following a seismic event can be expressed as (Utsu 1969;
433 Utsu & Ogata 1995):

434 $$\frac{dN(t)}{dt} \propto \frac{k}{(c+t)^p} \qquad (4)$$

435 Where $\frac{dN(t)}{dt}$ represents the aftershock frequency, *t* is the time from the mainshock-triggered
436 event, *k* is the productivity of aftershocks that depends on the total number of events, *p* is the
437 power-law exponent, and *c* defines the time delay before the onset of the power-law aftershock
438 decay rate and depends on the rate of activity in the earlier part of the seismic sequence. The
439 value of *c* is also related to the incompleteness of seismic catalogs after strong earthquakes.
440 Guo & Ogata (1997) obtained a range of *c* values between 0.003–0.3 days for various
441 earthquake datasets. In our simulation, the *c* value is fixed at 0.01 d. The value of *c* is selected
442 to be the lowest possible to obtain sufficient aftershock productivity in the very early part of
443 the aftershock sequence (Enescu *et al*., 2007; Kariche *et al*., 2018).

444 Based on the Nur and Booker (1972) hypothesis, the aftershock frequency rate within a
445 seismogenic volume can be proportional to the temporal evolution of pore-fluid pressure as :

446 $$\frac{dN}{dt} = \frac{1}{\alpha} \int \frac{\partial P}{\partial t}\, dv \qquad (5)$$

Where α is a constant that relate the rate of aftershock occurrence to the fluid pressure change $\frac{\partial P}{\partial t}$ integrated over a given volume v. In a 2-D fluid flow model, as developed by Nur & Booker (1972), the appropriate volume *v* defines the integration volume as the lower half-space. In our context, the term "appropriate volume" refers to the area where slip produces significant dilatation. *P* represents the pore-fluid pressure variation following an earthquake.

The model proposed here supposes that the high pore-fluid pressures are mainly concentrated in an area with low permeability that has the potential to maintain elevated pore pressure over time. For the Central Apennines and Ridgecrest aftershock sequences, the basic idea is that a transient pore pressure is created along a fault zone by the dilatancy–fluid diffusion mechanism. The slip phase leads to reduced fluid pressure along the fault plane, which is later restored during the drained fluid phase in response to the redistribution of fluid along the dilatant fault. The fault zone may act as a barrier and conduit of fluid simultaneously if we suppose an anisotropy of permeability. Regarding the structural aspect, fluid migration may take place through adjacent subsidiary fractures connected to bounding faults that are directly associated with earthquake and aftershock behavior (Kirkpatrick *et al.*, 2008; Kariche *et al*., 2018). Additionally, the arrangement of subsidiary fractures, their petrophysical properties, and other topological characteristics may create localized deformed zones that serve as barriers and fluid traps, leading to an accumulation of pore-fluid pressure (Yehya *et al.*, 2018).

The elevated pore-fluid pressure affects the effective normal stress and creates a zone of unstable sliding that controls the aftershocks' productivity. The thermal pressurization effect caused by the mainshock may also be viewed as a mechanism that generates elevated pore-fluid pressure over time. However, experiments conducted in freshly fractured rocks suggest that thermal pressurization might not offset the pore pressure changes caused by the dilatancy process (Brantut, 2020). This finding is further supported by theoretical studies on both mature and immature faults, which indicate that slip-induced dilatancy tends to dominate over thermal

pressurization effects (refer to Yamashita & Tsutsumi, 2018; Section 5.6). Consequently, it is plausible to consider the issue within a "steady-state" scenario, where the diffusion of pore fluid may act as a rate-controlling mechanism for the aftershock sequence.

Taking into account the boundary conditions for a steady-state source and assuming a one-dimensional Darcy flow, a simple poroelastic solution is given by Malagnini *et al*. (2012):

$$P(x,t) = (P_0 - P_1)erfc\left(\frac{x}{2\sqrt{ct}}\right) + P_1 \qquad (6)$$

Where *c* represents the value of fluid diffusivity and *erfc* is the complementary error function. For nucleation assisted by fluids, Abramowitz & Stegun (1970) wrote the *erfc* function as*:*

$$erfc\left(\frac{x}{2\sqrt{ct}}\right) = \frac{2}{\sqrt{\pi}}\int_{\frac{x}{2\sqrt{ct}}}^{\infty} e^{-\xi^2}\, d\xi \qquad (7)$$

In this case, the initial and boundary conditions may be posed as:

$$\begin{cases} P(x=0, t>0) = P_0 = \lambda_f\, \rho_r\, gz \\ P(x>0, t=0) = P_1 = \rho_w gz \end{cases}$$

Where ρ_r and ρ_w are respectively the rocks and fluid density, λ_f is the pore fluid pressure coefficient for an arbitrary depth and range between 0.6 and 0.8 for fault reactivation assisted by fluid (Rikitake 1972). Z represents the source depth and *g* the gravitational acceleration.

Replacing the 1D pore-fluid pressure form in the Nur & Booker (1972) equation with the complementary error function, a complete aftershock pore-fluid diffusion solution may be written as:

$$\frac{dN}{dt} = \frac{1}{\alpha}\frac{(P_0 - P_1)}{2\sqrt{\pi c t^3}}\int_0^{\infty} x\, e^{\left(-\frac{x^2}{4ct}\right)}\, dx = \frac{(P_0 - P_1)\sqrt{c}}{\alpha\sqrt{\pi}}\frac{1}{\sqrt{t}} \qquad (8)$$

490 This equation shows that in the presence of high pore-fluid pressure, the aftershock decay rate
491 is proportional $\frac{1}{\sqrt{t}}$. However, if an external source does not provide a sufficient fluid volume,
492 the change in pore pressure becomes non-stationary as time *t* elapses.

493 Considering the problem as non-steady, the pore pressure decays rapidly and would be one-half
494 of that associated with intermediate time scales. As a result, the decay in pore-fluid pressure is
495 counterbalanced by the redistribution of shear stress along the fault caused essentially by the
496 elastic fault's compaction (Biot, 1965; Booker, 1974; Brantut, 2020). Taking into account the
497 coupling between the pore pressure and the elastic stress (i.e., Coulomb's law), the productivity
498 of aftershocks over a large time scale can only occur if the time variation of shear stress exceeds
499 the time variation in shear strength along faults. Assuming an elemental length of fault rupture,
500 the aftershocks' decay rate may be seen as an integral of the time derivative of shear stress as:

501 $$\frac{dN}{dt} = \int_{-1}^{1} \frac{\partial}{\partial t}\, \tau_{xz}\,(x,t)\, dx \qquad (9)$$

502 If we consider the hypothesis that aftershock production is essentially driven by stress load due
503 to the fault compaction, the stress state along small-scale ruptures may be expressed as (Booker,
504 1974):

505 $$\tau_{xz}(x,t) = \frac{-H(t)}{\pi(1-x^2)}\,[1-\beta\, F(x,t)] \qquad (10)$$

506 where: *H (t)* represents the Heaviside step function, β is the value of compressibility during the
507 relaxation process, where the fluid is assumed to play no role, and F (t, x) is an analytic function
508 defined as (Booker, 1974):

509 $$F(x,t) = 2t\left\{\frac{1+x}{(1-x)^2}\,\left[1-e^{\left(-(1+x)^2/4t\right)}\right] + \frac{1-x}{(1+x)^2}\left[1-e^{\left(-(1+x)^2/4t\right)}\right]\right. \qquad (11)$$

Based on Equations 9, 10, and 11, the long-term decay of aftershock frequency, associated with the stress redistribution along fractured rocks, can be described by Booker's approximation as follows:

$$\frac{dN}{dt} = \frac{1}{4}\left(1 - e^{-4/t}\right) + \lim_{\xi \to 0} \frac{1}{\xi^2}\left[1 - e^{-\xi^2/t}\right] \simeq \frac{1}{t} \qquad (12)$$

This solution indicates that, for a sufficient duration of time, the aftershock frequency decay resulting from the pore-pressure drop and the redistribution of shear stress along fractures would replicate the Omori-type signal.

3. Modeling Fault Interactions and Fluid Effects

To compute a static stress change caused by major earthquakes on nearby fault ruptures, I use the concept of Coulomb stress change on a fixed receiver fault. The applied stress change, calculated as the Coulomb Failure Function (ΔCFF; e.g. Reasenberg & Simpson, 1992), is expressed by:

$$\Delta CFF = \Delta\tau - \mu\,(\Delta\sigma_n - \Delta P) \qquad (13)$$

Where τ is the shear stress, σ_n is the normal stress (compression positive), P is the pore-fluid pressure, μ' is the coefficient of internal friction, and Δ refers to changes during the earthquake. The second term in Equation (13), defining the Terzaghi effective normal stress, may be replaced by the notion of effective friction coefficient as:

$$\Delta CFF = \Delta\tau - \mu'\Delta\sigma_n \qquad (14)$$

The apparent (or effective) friction μ' is given by Reasenberg & Simpson (1992) as follows:

$$\mu' = \mu\,(1 - B) \qquad (15)$$

where μ is the friction coefficient and B is the Skempton coefficient, which defines the relationship between the stress change and pore pressure change (Rice & Cleary, 1976; Beeler et al., 2000).

538

539 At the intermediate between undrained and drained fluid phases, the Skempton coefficient
540 B may be related to the undrained and drained state of fluids as (Yamashita & Tsutsumi, 2018):

541 $$\frac{K}{K_u} = 1 - \alpha B$$

542 Where α is called the Biot & Willis coefficient (Biot, 1965) and represents the ratio
543 between the increment of fluid content and the volumetric strain change following an
544 earthquake. K and K_u represent the drained and undrained bulk moduli, respectively, and may
545 be written as a contribution of undrained (υ_u) and drained (υ) Poisson ratios (Yamashita &
546 Tsutsumi, 2018a):

547 $$\frac{K}{K_u} = \left(\frac{1+\upsilon}{1+\upsilon_u}\right) \times \frac{\upsilon_u}{\upsilon}$$

548 If an isotropic poroelastic model is assumed (Beeler et al., 2000), an intermediate short-term
549 poroelastic solution can be obtained by combining shear, normal, and pore-fluid contributions
550 as:

551 $$\Delta CFF = \Delta\tau - \mu\,(\Delta\sigma n - \frac{(\upsilon_u - \upsilon)}{\alpha\,(1-2\upsilon)(1+\upsilon_u)}\,\Delta\sigma_{kk}) \qquad (16)$$

552 Equation (16) demonstrates that the influence of pore fluids is not maximized during the
553 undrained phase but becomes significant as the system transitions toward the drained phase.
554 This behavior has been previously investigated by Segall and Rice (1995) and Chambon and
555 Rudnicki (2001), who explored stress changes resulting from fault geometries using a spring-
556 slider model applied to dilating, fluid-saturated faults.

557 In cases where rocks are fully saturated and exhibit a high density of pre-existing fractures
558 $(\upsilon_u, \upsilon) = 0.31, 0.15$ (Rice & Cleary, 1976; Bosl & Nur, 2002), the average poroelastic stress
559 response on target faults is approximately 40% greater than the Coulomb stress modeled using
560 only the elastic properties of the upper crust. Based on this fact, the presence of fluids along the

561 fault zone results in a short-term coupled poroelastic response that enhances stress loading on
562 fixed receiver faults. This occurs particularly in regions where fluid diffusion increases pore-
563 fluid pressure over time.

564 However, the absence of a fully realized 3D poroelastic model limits the ability to
565 physically characterize the complex and complete processes of fluid diffusion along active
566 faults. To address this, the cumulative stress change associated with the full poroelastic
567 relaxation following an earthquake is modeled using analytical 3D poroelastic solutions derived
568 from 3D elastic modeling. This approach incorporates the temporal variation of the Poisson
569 ratio as fluids transition from an undrained to a fully drained state (Segall, 2010, Sect. 10.7).
570 Rather than being an oversimplification, this methodology compares elastic deformation
571 scenarios between the "undrained" fluid state (immediately after the earthquake) and the fully
572 "drained" state (when fluid redistribution and heterogeneous fluid pressure equilibrium are
573 established along the fault zone). While it does not explicitly explore the detailed temporal
574 evolution of fluid migration and crustal deformation, the variation of the Poisson ratio from the
575 undrained to drained states is interpreted as a consequence of changes in rock rheology driven
576 by fluid drainage along the fault zone.

577 **RESULTS AND ANALYS**

578 **1. TEMPORAL VARIATION OF B VALUE, FORESHOCK ANALYSIS AND THE**
579 **ROLE OF FLUID**

580 Figure 4 shows the preferred b-value time series for the Ridgecrest case. The optimum time
581 series calculation is made with a sample size of 250 events at a low window overlap (~4%).
582 The temporal evolution of the earthquake size distribution shows an increase in b-value one
583 year before the 2019 Ridgecrest sequence followed by a gradual decrease in b-value ~ one
584 month before the Mw 6.4 foreshock (Figures 4; 5 and S7A). After the Mw 6.4 earthquake, the

585 b-value rapidly varies from minimum to maximum and from maximum to minimum just before
586 the Mw7.1 earthquake showing major double peaks (Figures 4C and 5A) as predicted by the
587 laboratory experiments in water-saturated specimens (e.g., Main et al., 1989). The recovery in
588 b-value before the Mw 7.1 earthquake as observed in Figures 4 and 6A is interpreted here as a
589 response to pore pressure drop during the undrained phase of the fluid. This value is close to
590 the value of b ~ 1 during the left-lateral earthquake but the increase in foreshocks productivity
591 caused by fluid migration and pore pressure instability in the ~ 33 hours preceding the Mw7.1
592 right-lateral earthquake tends to re-decrease the b-value to ~ 0.5 creating a double b-value
593 minimum as observed in Figures 4C, 5A, 5C, and 6A.

594 The Mw 7.1 shear rupture is accomplished by evolving the ensemble of foreshock events
595 off the Mw6.4 main rupture. This may be represented by a highly oriented diffusive seismicity
596 that grows in a shear zone of intense deformation. Therefore, the Mw7.1 dynamic failure does
597 not occur at peak stress (Figure S13A) and the failure process seems to be more dependent on
598 the temporal evolution of seismicity and related pore-fluid pressure redistribution nearby the
599 Mw7.1 nucleation area (Figure S13C) rather than the variation in elastic stress. In this case, the
600 minimum doublet b-value as observed in the b-value time series may be interpreted as a local
601 dilatancy hardening phase resulting from fluid migration along conjugate fault ruptures. At this
602 time, the fluid migration at a short time scale requires a significant evolution of the permeability
603 along fault ruptures. Based on this assumption and other considerations in relation to the stress
604 change induced by fault geometries in a spring-slider model for dilating fluid-infiltrated fault
605 (Segall & Rice, 1995; Chambon & Rudnicki, 2001), the temporal fluctuation of the b-value
606 related to the 2019 Ridgecrest sequence seems to be controlled by slip instability due essentially
607 to the pore pressure fluctuation caused by fluid migration along the heterogeneous fault zone.
608 The temporal b-value instability associated with the pore pressure fluctuation continues during
609 the two months following the Mw7.1 earthquake (Figures 4B and C). The ~ two-month

instability period may also represent the duration of the Mw 7.1 poroelastic rebound. Also, the similarities between the temporal evolution of the b-value for the 2019 Ridgecrest and the 2016 Amatrice-Norcia sequences (Figures 6A, 6B and S13) may suggest an analogous physical mechanism controlling the foreshock occurrence for both sequences.

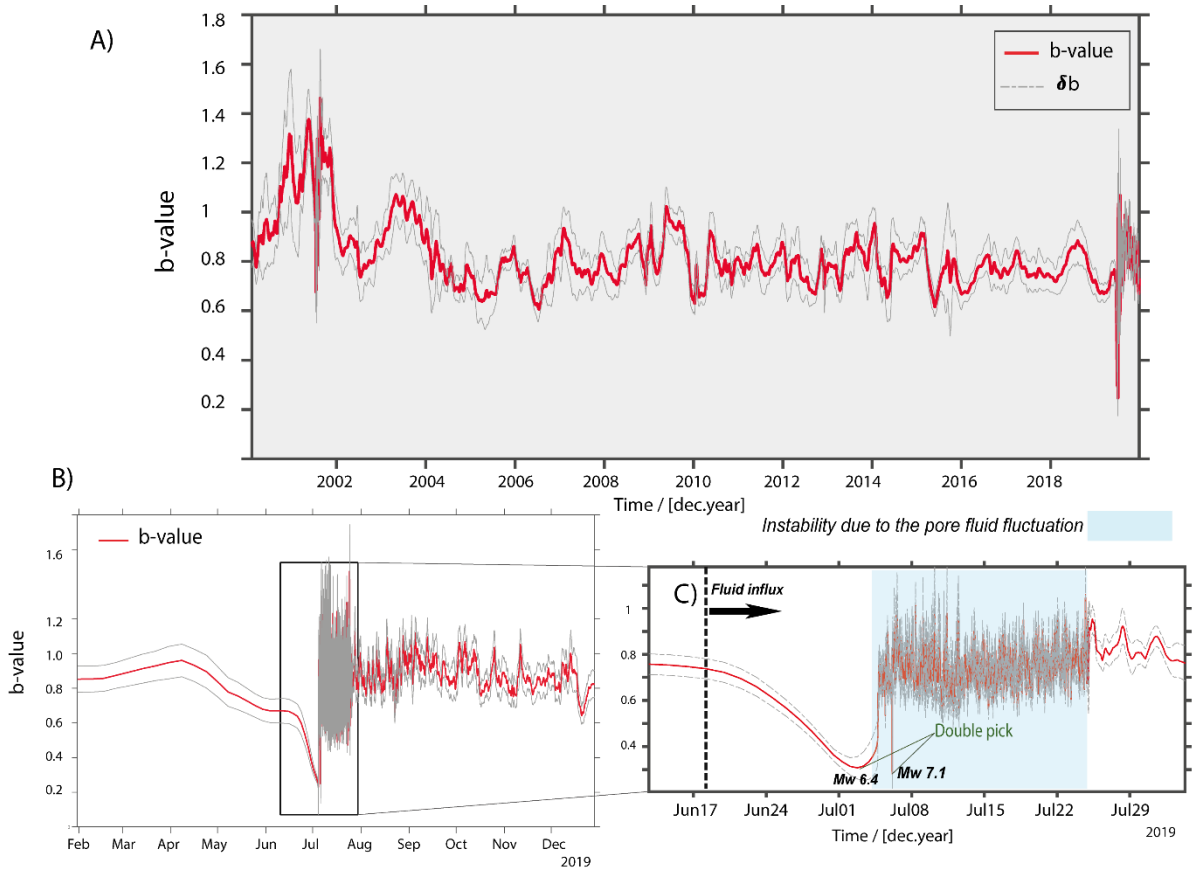

Figure 4*: Earthquake size distribution estimates for the Ridgecrest fault zone area.* ***A)*** *b-value time series spanning the period from 2000 to 2020. The b-value time series were computed using the maximum curvature approach for a moving window of 250 events with a step size of 50 events. The window overlap is fixed at ~4%. The Standard deviation of the b-value (δb) is represented by a dashed grey line and is obtained using the maximum likelihood estimation approach (Shi & Bolt 1982).* ***B)*** *Zoom-in figure for the period from February 2019 to January 2020.* ***C)*** *Zoom-in figure for the period from ~ 2 weeks before the 2019 Mw 6.4 first earthquake to August 01, 2020, but by adding a high smoothing plot factor (~ 6) to the b-value estimations.*

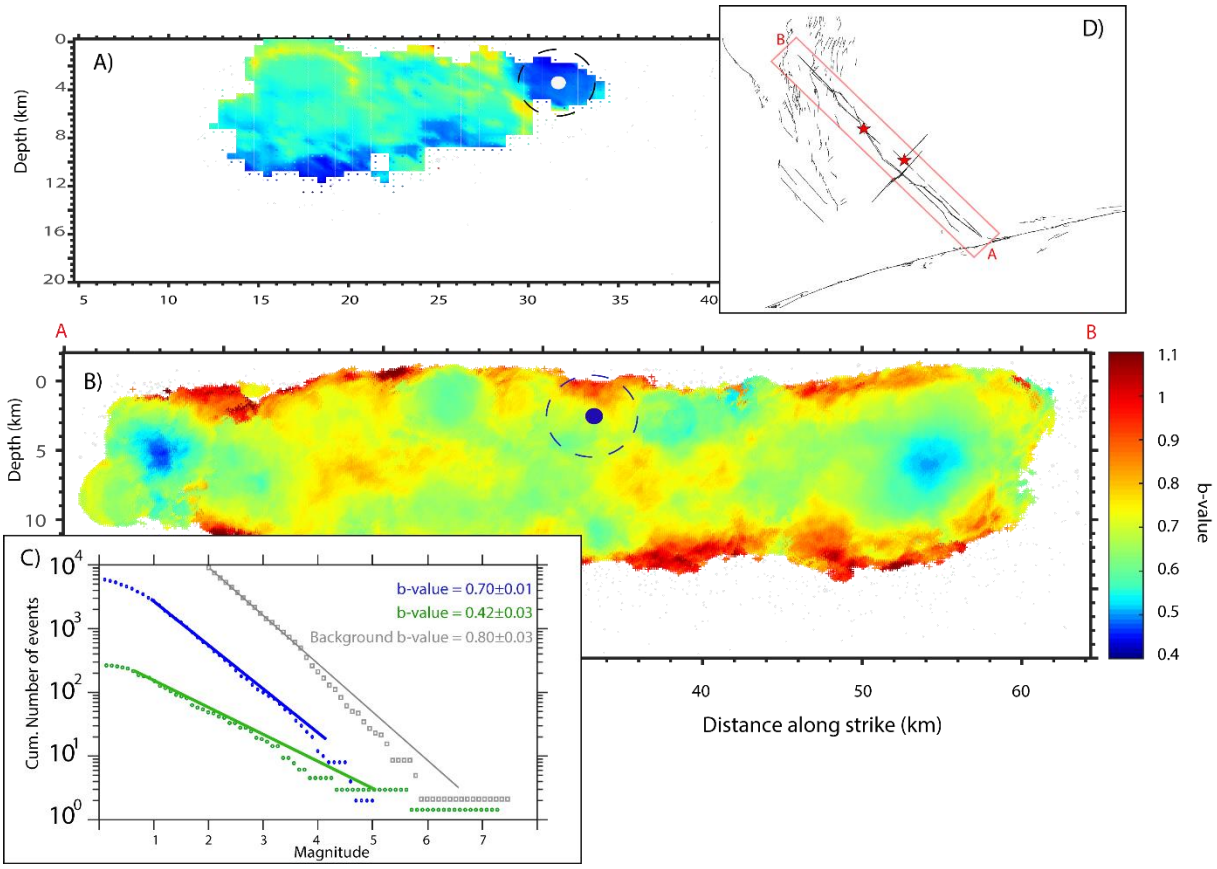

Figure 5*: Spatio-temporal evolution of the b-value associated with the 2019 Ridgecrest sequence:* ***A)*** *cross-section showing b-value distribution before the Mw7.1 earthquake.* ***B)*** *Cross-section showing a b-value distribution after the Mw7.1 earthquake.* ***C)*** *Frequency-Magnitude Distributions (FMD) around the Mw7.1hypocentral area before and after the Mw7.1 event: the green curve represents the G-R distribution before the Mw7.1 event, the blue curve represents the G-R distribution after the Mw7.1 and the gray curve represents the background FMD distribution. The dashed colored circles in A) and B) represent the locations of events used in C).* ***D)*** *Position of the cross-section with respect to the surface distribution of the Ridgecrest fault ruptures. The Ridgecrest Fault-ruptures are from Xu et* al., (2020)*. The Quaternary faults are from the USGS.*

The double b-value minima as observed in Figure 6B correlates with the relative crustal velocity fluctuation observed in Amatrice-Norcia seismogenic zone (Soldati *et al.*, 2019). Note that the difference between Figure 4C and 6A in the 2-3 weeks preceding the Mw 6.4 earthquake is attributed to the use of a higher smoothing factor. The smoother curve in Figure 4C is employed solely to distinguish between the high and low-frequency b-value time series, thus

638 providing more accurate estimates of the temporal instability associated with the pore fluid
639 fluctuations. It is noteworthy that the b-value time series with a double b-value minimum
640 shown in Figure 4 is consistent with the b-value estimates obtained taking into account the Mc
641 values obtained by the Lilliefors test (Table 1; also refer to the "ANALYSIS AND
642 ROBUSTNESS OF THE B-VALUE AND MC" section in the Supplementary Material).
643 Additionally, the b-value mapping in Figure 5 aligns with the estimates derived from the EMR
644 technique proposed by Nanjo (2020) for the same sequence, particularly during the period
645 preceding the Mw 7.1 event. The key difference is that Nanjo (2020) exclusively uses a static
646 elastic stress change modeling procedure to explain the observed low b-value near the Mw 7.1
647 nucleation zone.

648 Considering the case of the 1997 Colfiorito sequence, the gradual decrease in the b-value
649 prior to the foreshock sequence (Figures 7C and 7D) seems to be concordant with the fracture
650 model of Main *et al*. (1990). Adopting the Main *et al.* (1990) experimental model of cracks, the
651 temporal evolution of the b-value may be defined here as a rapid failure after periods of strain
652 hardening and strain softening due essentially to the pore-fluid diffusion process. The dilatancy
653 softening phase related to the 1997 Colfiorito sequence seems to be controlled by the fluid
654 migration along fault zones where the stress intensity is highly coupled to the temporal variation
655 in effective normal stress. Considering the Terzaghi Law, the fluid diffusion phase will play a
656 crucial role in accelerating seismicity by decreasing the magnitude of effective normal stress
657 acting along cracks, promoting the occurrence of fast slip episodes at short time scale.

658 The time evolution of the b-value following the 2009 L'Aquila sequence differs from those
659 obtained for the 2016 –Amatrice-Norcia and the 2019 Ridgecrest sequences (Figures 6 and 8).
660 This difference may be due to the presence of a large deep fluid reservoir near the L'Aquila
661 fault zone which maintains a high pore fluid pressure during a large period of time. In fact,
662 InSAR time series analysis related to the central Apennine earthquakes reveals that the

663 sedimentary basin nearby the L'Aquila fault zone had experienced about 10 mm of accelerating
664 subsidence in the years prior to the L'Aquila mainshock (Moro *et al.* 2017) in agreement with
665 the observed change in the frequency of the b-value time series (Figure 8).

666 The accelerating subsidence is viewed as a consequence of large pre-earthquake fluid
667 migration along the fault zone (Moro *et al*. 2017). Based on our estimation of the b-value
668 (Figures 7 and 8) and ground deformation estimated from SAR imagery (Moro *et al*., 2017),
669 the acceleration of subsidence is interpreted here as probably due to large dilatancy-fluid
670 diffusion processes that control the temporal fluctuations of the b-value at a large time scale.
671 The analysis of the time-magnitude series shows a gradual decrease in the number of events
672 with magnitude $M < 3$ associated with an increase of events with magnitude > 3.5 in agreement
673 with the change in the b-value time series (Figures 7 A and 8). A second phase with an apparent
674 increase of small magnitude earthquakes accompanied by a decrease in the number of events
675 with a magnitude Mw larger than 3.5 is observed in the two months prior to the 2009 L'Aquila
676 mainshock (Figures 7 A and 8). The gradual increase of micro-seismic events observed in the
677 two months prior to the L'Aquila mainshock is highly coupled with the gradual decrease in the
678 b-value (Figure 8; Figures S3A and B).

679 The trend of the b-value time series during the last phase of the L'Aquila interseismic
680 period is understood here as an influx of pore fluid into a dilatant volume near the nucleation
681 zone. The increase in the magnitude of foreshocks just before the L'Aquila mainshock (Figure
682 8) considerably affects the temporal evolution of the b-value by creating a sudden drop in the
683 b-value. The time delay between the start of foreshocks and the b-value decrease seems to
684 correlate with the gradual increase in microseismic events followed by a sudden increase in
685 earthquakes with magnitude $M \geq 3.0$ (Figure 8). This temporal-spatial clustering of seismicity
686 may suggest a complex stress evolution, consistent with a heterogeneous effective stress drop
687 modulated by fluid migration within a structurally anisotropic fault zone.

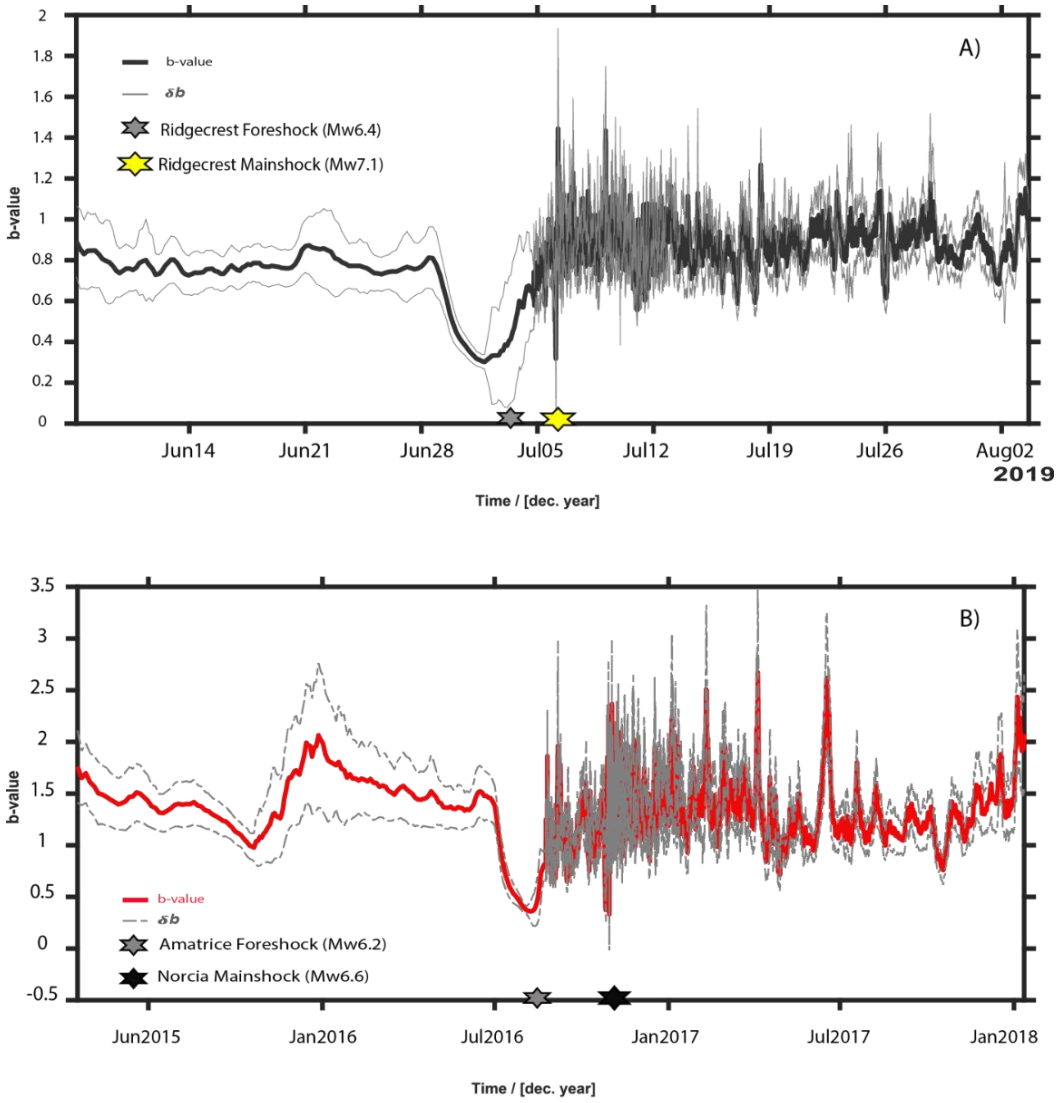

688

689 **Figure 6***: Comparison between b-value time series analysis following:* ***A)*** *2019 Ridgecrest sequence*
690 *and* ***B)*** *2016 Amatrice-Norcia sequence. The two figures show a double pick during the foreshock –*
691 *mainshock period as predicted by the laboratory experiments on water saturated specimens. The b-*
692 *value time series is performed using the combined high resolution NEIC-USGS catalogs and*
693 *supplemented by the Shelly (2020) catalog for events that occurred during the 2019 Ridgecrest*
694 *foreshock-mainshock sequence. The b-value time series for the 2016 Amatrice-Norcia sequence is*
695 *performed using the entire catalog of the INGV combined with the local catalogs published by Tan et*
696 *al. (2021). The b-values time series are computed using ZMAP7.0. For both sequences, the uncertainty*
697 *estimation is obtained by 100 bootstraps related to windows size of 250 events.*

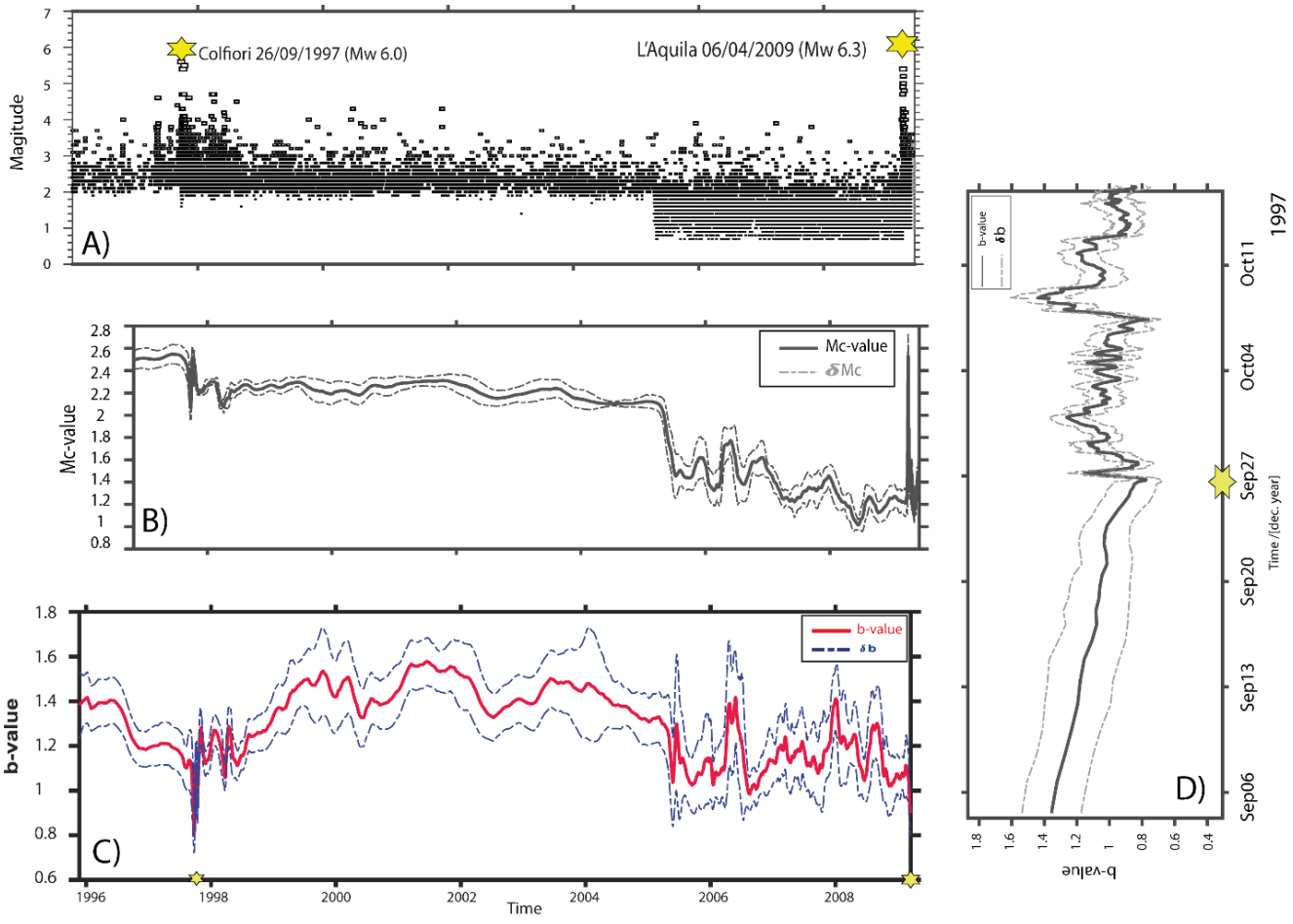

Figure 7. ***A)*** *Earthquake magnitude versus time for the central Appennines covering the periods between 1996 to 2009 and using combined catalogs of INGV and Gasperini et al (2013) catalogs. The yellow stars represent the position of the 2019 Mw 6.0 Colfiorito and the Mw6.3 L'Aquila mainshocks.* ***B)*** *Mc-value time series using the same catalogs as A) and covering the periods between 1998 to 2009. The magnitude of completeness (Mc) varies in times from 2.5 (before 1997) to 1.4 (after 2005) with uncertainties δMc equals to 0.15 and 0.18 respectively.* ***C)*** *Temporal evolution of the G-R b-value in the central Appennines covering the same periods as in A.* ***D)*** *temporal evolution of the G-R b-value before and during the 1997 Colfiorito sequence. The b-value computation is resolved by using a coherent level of Mc equal to 2.5 ensuring a stable state over time and thereby minimizing b-value artifacts. The yellow star indicates the location of the Mw 6.0 event. It is worth noting that the trend observed in the b-value time series, as discussed in C), and incorporating temporal variations of Mc, closely mimic the results obtained when assuming a fixed Mc value of 2.5 and employing N~250 fixed sample size windows with 100 bootstraps.*

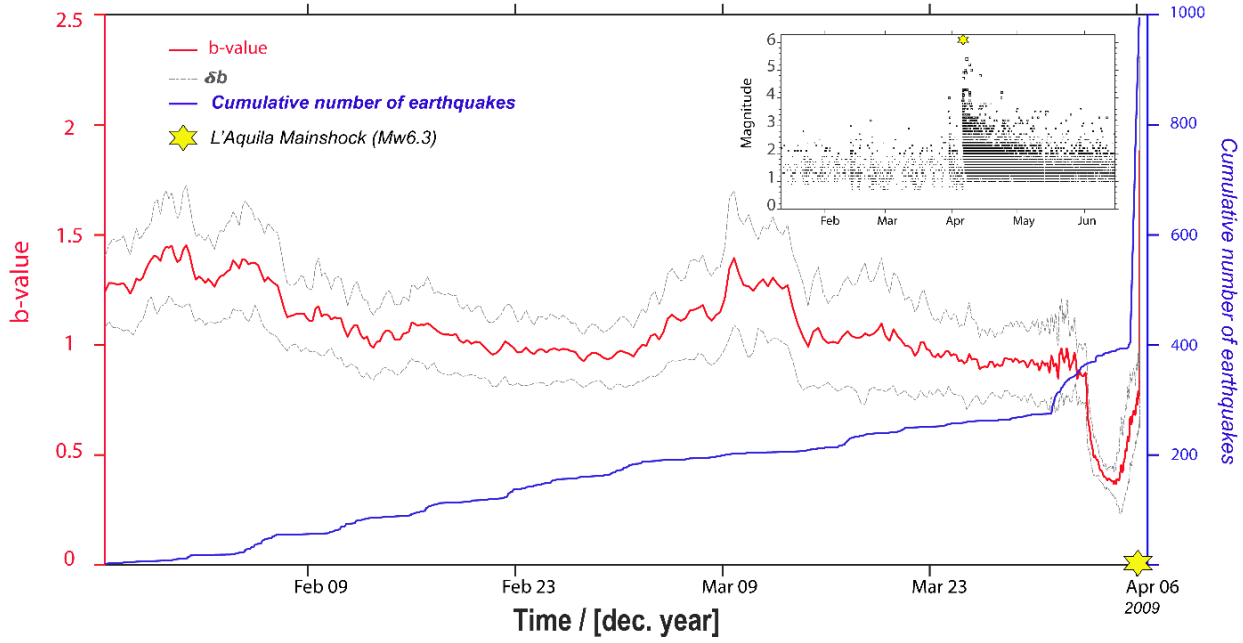

Figure 8 *Temporal evolution of the G-R b-value (in red) and the cumulative number of earthquakes (in blue) during the Foreshock period priors to the Mw6.3 L'Aquila earthquake using the entire catalogs of Gasperini et al (2013). The b-value time series is obtained using a sample windows size of 150 events with 100 bootstraps. For safety, the Mc correction value is fixed at 0.2 comparable to the value used by the predictive foreshock model of Gulia et al (2016). The black stars represent the position of the Mw 6.3 L'Aquila mainshock.*

2. STRESS CHANGE, POROELASTICITY AND TEMPORAL EVOLUTION OF AFTERSHOCK

As shown in the previous section, the occurrence of moderate to strong earthquakes along the SWL-ECSZ and Central Apennines zones may be coupled with the fluid migration along heterogeneous fault zones. This fluid migration can lead to abnormally elevated pore pressure and promote the occurrence of moderate to large earthquakes. Based on the Coulomb failure stress hypothesis, the post-seismic poroelastic stress change modeling following the Ridgecrest Mw 6.4 left-lateral event shows a high value of stress along the Mw7.1 right-lateral rupture

(Figures 9A and S13; Kariche, 2022) when the purely elastic stress modeling predicts an absence of earthquake activities (Figures 9B and 9C; Lozos & Harris, 2020; Kariche, 2022). The stress change modeling result in Figure 9A illustrates the post-seismic poroelastic stress change scenario based on the assumption of cumulative poroelastic stress responses resulting from changes in drained and undrained Poisson ratios. It also incorporates a significant Skempton coefficient value (B>0.5) (For a comprehensive understanding, refer to Section 3 of "METHODOLOGY AND DATA" and Section 3 in Kariche, 2022). Subsequently, the study compares the poroelastic stress response to the temporal evolution of poroelastic stress changes that occurred following the Mw6.4 foreshock on the receiver fault plane responsible for the Mw7.1 event. This comparison is made by employing different values of fluid diffusivity, as depicted in Figure S13. The Coulomb stress change modeling (as illustrated in Figure S13) considers a time-dependent pore-fluid pressure change derived from the solution proposed by Piombo *et al*. (2005). In this modeling approach, a permeable source fault is assumed to be associated with the Mw6.4 event. In contrast, the conjugated receiver fault plane in relation to the Mw 7.1 nucleation area is considered as a barrier to the fluid flow.

Considering the diffusive effect of fluid, the Coulomb stress change modeling shows a stress increase on the fault plane responsible for the Mw 7.1 earthquake (Figures 9A and S13C), where the coseismic Coulomb stress change expects a negative (or insufficient) stress value (Figures 9B and C). One of the possible explanations for the temporal evolution of stress change values from negative to positive, as shown in Figures 9 and S13C, is the fluid redistribution along conjugated fault ruptures, which creates favorable conditions for a weakening mechanism by increasing pore-fluid pressure along the right-lateral fault rupture and, in fact, promoting the occurrence of the Mw7.1 earthquake. The rupturing process on conjugated strike-slip faults assisted by fluid migration is not unusual. Using a typical undrained and drained Poisson ratio for a Berea sandstone, the modeling of the Coulomb failure function per unit of stress drop

caused by the 1987 Elmore Ranch event (Mw 6.2) on the conjugated Superstition Hills fault (Mw 6.6) shows a maximum poroelastic stress value in the ~11 hr following the Mw 6.2 event (Hudnut *et al*., 1989). For the 2019 Ridgecrest sequence, the Coulomb stress change modeling, taking into account the effect of fluids, reveals that the ~33 hr time delay between mainshocks may be viewed as a triggering mechanism controlled by the fluid-flow process (Figures 9A and S13; Kariche, 2022). The value of fluid diffusivity is relatively low compared to the value obtained for the Superstition Hills sequence and may suggest that the fluid migration along faults controls the delay between earthquakes. Note that the coseismic (undrained) isotropic elastic stress change models, illustrated in Figures 9B and C, are undertaken primarily for comparative purposes. They serve as a basis for comparison against the outcomes of short-term poroelastic stress change modeling.

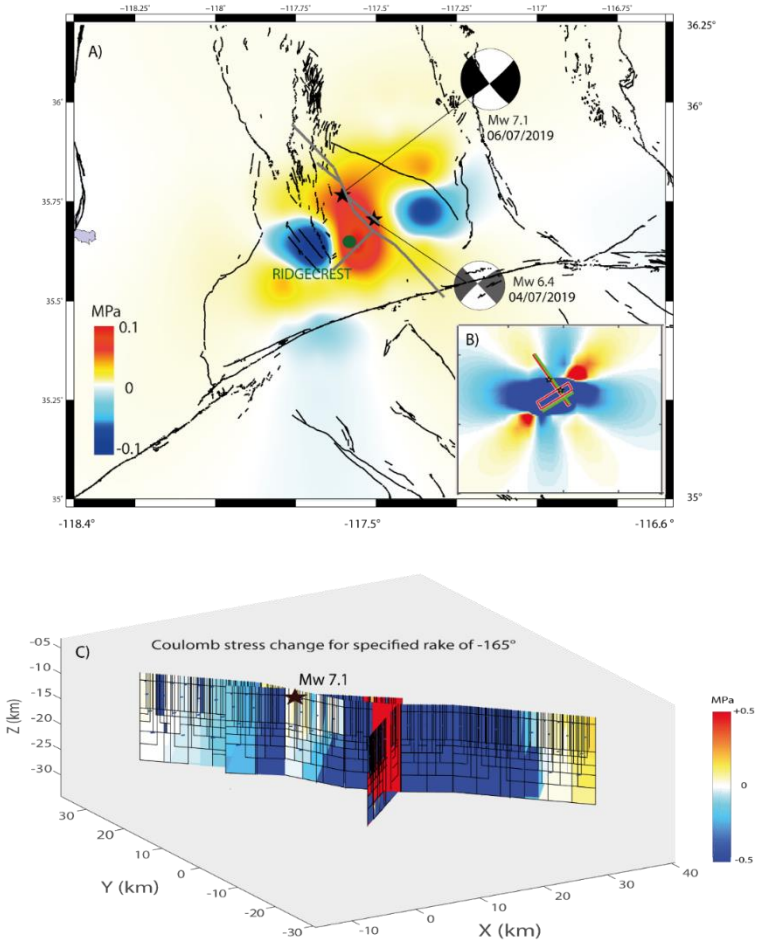

Figure 9: ***A)*** *Short–term poroelastic stress change modeling following the Mw6.4 earthquake on receiver fault planes with Strike /Dip/ Rake = 143°/85°/-165° at 8km depth. The post-seismic stress redistribution following the 04-07 (Mw6.4) from the undrained state to the drained fluid state using extreme undrained and drained Poisson ration values (υu, υ = 0.31, 0.15). These values are interpreted as a consequence of a high variation in rock rheology before and during the Mw6.4 earthquake. The 2019 Ridgecrest surface rupture faults are from Xu et al (2020). The grid depth is selected with respect to the Mw 7.1 hypocenter location of* Wang et al., (2020). ***B)*** *Co seismic stress transfer caused by the Mw6.4 earthquake on receiver fault planes with Strike /Dip/ Rake = 143°/85°/-165 at 8 km depth. The co-seismic stress modeling is performed using simple conjugate fault geometries. C) Co-seismic stress change caused by the Mw 6.4 left lateral rupture on the Mw 7.1 right lateral fault plane. The Mw 6.4 complex geometry and slip distribution are from Xu et al (2020). The Coulomb stress change modeling was performed for a fixed rake of –165°. The black star represents the same location of the Mw 7.1 event as in figure 5.*

Fluid migration during an earthquake may also impact the frequency of aftershocks. Figure 10 illustrates the cumulative stress change modeling resulting from the complete poroelastic relaxation of the Mw 7.1 Ridgecrest earthquake using different values of drained υ and undrained υ_u Poisson ratios, in comparison to the spatial distribution of aftershocks following the Mw7.1 Ridgecrest earthquake. Figures 10 (A, B, and C) reveal a correlation among: 1) the evolution of stress change following the Mw 7.1 earthquake, 2) the fluid diffusion process, and 3) the spatial distribution of a subset of aftershocks near and NNW of the Mw7.1 epicenter. The values of υ_u and υ used in Figure 10 might be associated with water-saturated rocks in the upper few kilometers of the seismogenic zone ($h \leq 15$ km). The fluid-diffusion process within the context of the 2019 Ridgecrest sequence appears to primarily operate at a local scale (Figures 9 and 10). The Coulomb stress change modeling, which incorporates the diffusive effects of

790 fluids, reveals a clear increase in stress change values near the epicentral region of the Mw 7.1
791 event (Figure 9A). Furthermore, the full poroelastic relaxation resulting from the Mw7.1 event,
792 particularly along faults parallel to the main rupture, seems to correspond to the spatial
793 distribution of aftershocks in the northern part of the Mw7.1 main rupture (Figures 10A, B, and
794 D).
795 In contrast, for the southern section of the Mw 7.1 Ridgecrest fault zone, the triggering
796 mechanism seems to operate independently of the fluid diffusion process (Figures 10A, B, C
797 and Figure S14). These findings support the idea that the generation of aftershocks following
798 the 2019 Ridgecrest earthquake is complex and may be related to both afterslip and poroelastic
799 relaxation processes. Indeed, an analysis of the co-seismic and early post-seismic surface
800 deformation (~2 months of deformation) following the 2019 Ridgecrest event suggests that the
801 observed post-seismic deformation during the first month may result from a combination of
802 afterslip and poroelastic rebound (Wang & Bürgmann, 2020). Based on the surface deformation
803 analysis (Wang & Bürgmann, 2020) and stress change modeling results (Figure 10), it is
804 reasonable to propose that the seismicity rate in the southern part of the Mw 7.1 main fault is
805 primarily driven by a model based on the evolution of afterslip, a conclusion supported by time
806 series analysis from the B921 strainmeter located in the same area (Hirakawa & Barbour, 2020).
807 Conversely, the early generation of aftershocks in the northern part appears to be predominantly
808 influenced by the poroelastic rebound resulting from the Mw 7.1 mainshock.

809 To explore the detailed mechanism of post-seismic deformation following the 2019
810 Ridgecrest sequence and related fluid migration, I analyze the temporal evolution of the
811 aftershock frequency rate associated with the Mw 7.1 earthquake and compare it with the case
812 of the Central Apennines. Figure 11 shows a comparison between the effect of fluid
813 redistribution on aftershock occurrence following the Mw 6.0 Colfiorito and the Mw 7.1
814 Ridgecrest earthquakes.

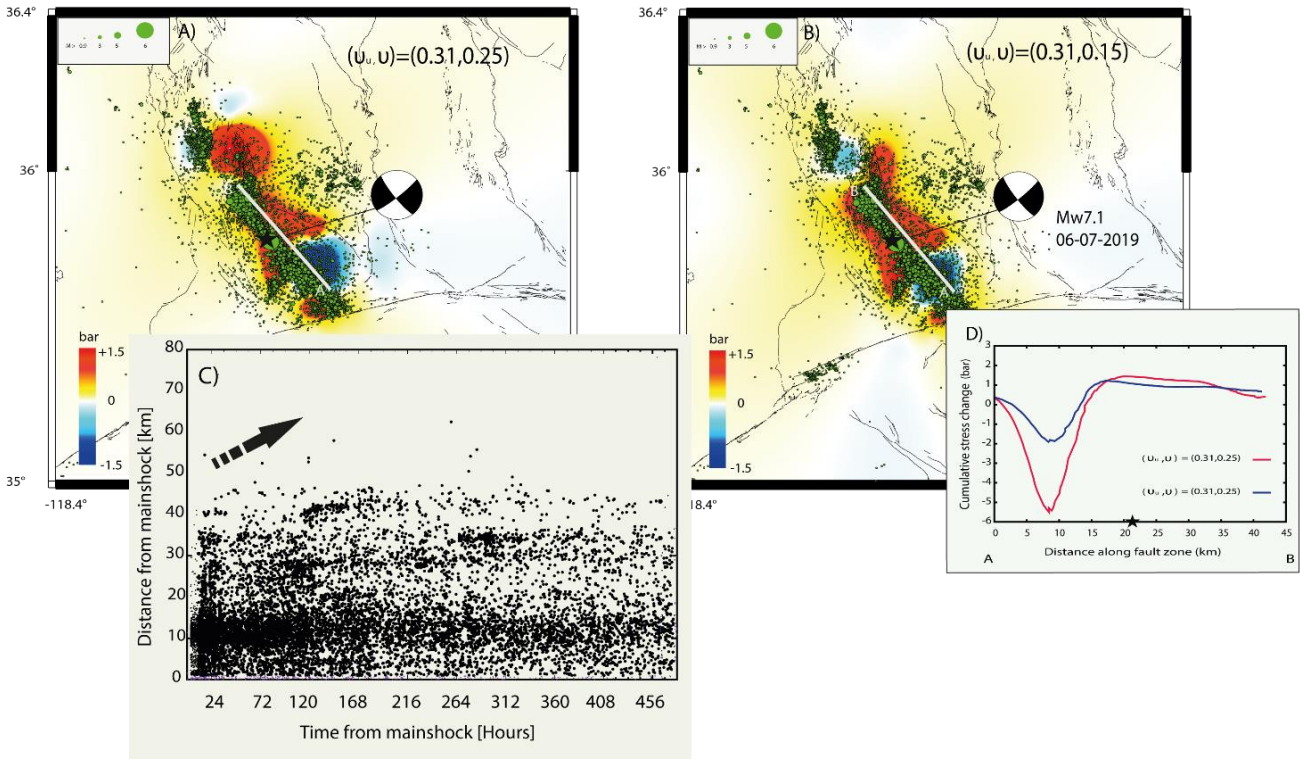

Figure 10: *Cumulative stress change due to the full poroelastic rebound following the Mw7.1 Ridgecrest earthquake on right lateral fixed receiver fault planes parallel to the Mw7.1 main rupture.* ***A)*** *poroelastic stress change modeling using a typical value of undrained and drained Poisson ratio(υu,υ)=(0.31,0.25).* ***B)*** *poroelastic stress change modeling using the extreme value of undrained and drained Poisson ratio (υu,υ)=(0.31,0.15).* ***C)*** *Spatiotemporal evolution of seismicity during the ~20 days following the Mw7.1 mainshock. The triggering front is represented as a time-distance plot of the events occurring from the Mw7.1 epicenter to the Coso geothermal area. D) Poroelastic stress change profiles caused by the full relaxation of the Mw7.1 earthquake along parallel right-lateral fault ruptures. The seismicity databases are from NEIC-USGS. The stress change modeling is fixed at 8 km depth. The black arrow in Figure C indicates the average direction of seismicity migration.*

Figure 11 (A and C) shows strong similarities between the temporal evolution of the aftershock sequence following the two earthquakes. The aftershock frequency rate curve starts

with a rate decay of $1/\sqrt{t}$, while it becomes equal to $1/t$ in days to one month after the 1997 Colfiorito and Mw 7.1 Ridgecrest mainshocks as predicted by the pore-fluid diffusion equation (see equation8 in the methodology section; Figures 11A and C).

Based on the pore fluid flow hypothesis, the $1/\sqrt{t}$ decay is interpreted as an increase in aftershock productivity due to the pore fluid diffusion along the fault zone. The increase in aftershock productivity is also observed in Omori fit curve when the seismicity rate shows additional aftershocks in the ~10–20 days after the Mw 6.0 Colfiorito and in the ~5–20 days after the Mw 7.1 Ridgecrest mainshock (Figures 11B and D), which cannot be explained by the aftershock rate decrease as predicted by the Omori Law. These results are also supported by the abnormalities in aftershock activity observed during monitoring of the temporal and spatial seismic activity following the Mw 6.4 Ridgecrest earthquake (Ogata & Omi, 2020). In addition, the duration of the increase in aftershock activity (Figure 11D) seems to follow the duration of pore-fluid instability as estimated by the b-value time series (Figure 4C). Note that the underproduction of aftershocks as seen just after the Mw7.1 mainshock (Figure 11C) may be due to the under-reporting of small events in relation to the incompleteness of the seismic catalogs soon after the mainshock.

The aftershock frequency rate curve (Figure 11A) also mimics the 1 km/day migration of seismicity toward the southeast following the Mw 6.0 mainshock (Figure 1b in Catalli *et al.,* 2008). For the Ridgecrest sequence, the spatiotemporal analysis of the aftershocks indicates a migration rate of ~4 km/day in the northern part of the Mw 7.1 event (Figure 10C, Figure 12). Based on the pore pressure-diffusion propagation solution in an effective isotropic homogeneous poroelastic medium (Shapiro, 2015, *Ch 3, Sect 3.3*), the shape of the pressure front that best matches the 4 km/day aftershock migration rate is achieved by considering a high fluid diffusivity value of 275 m^2/s (Figure 12B).

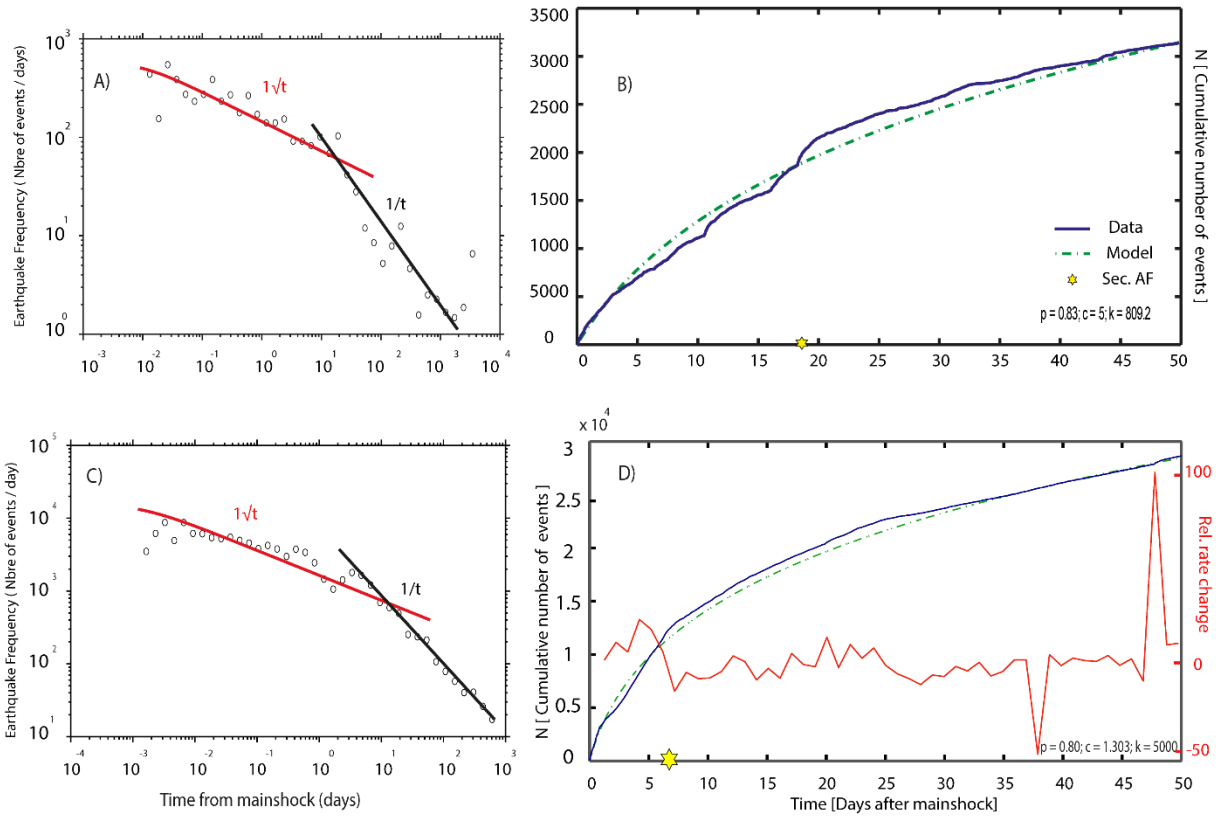

Figure 11: *Representation of the temporal postseismic effect following the Mw 6.0 Colfiorito and Ridgecrest earthquakes.* ***A)*** *Seismicity rate change versus time following the Mw 6.0 Colfiorito earthquake.* ***B)*** *Comparison of observed seismicity (blue) and the Omori fit (green) using the Zmap algorithm for 50 days' time windows following the Mw6.0 Colfiorito mainshock.* ***C)*** *Seismicity rate change versus time following the Mw 7.1 Ridgecrest earthquake.* ***D)*** *Comparison of observed seismicity (blue) and the Omori fit (green) following the Mw7.1 Ridgecrest mainshock using the Zmap algorithm for 50 days' time windows. For the aftershock frequency vs time curves, the value of c is fixed to 0.01 d for Panels A and C and suppose variable (from 2.4 to 5) for Panels B and D. The yellow stars represent the position of the second major choc for each sequence. The relative earthquake rate change (red curve in D) is obtained from the change in slope of the cumulative number curve using a Habermann function regardless of the time of greatest change and comparing the rate in the two parts of the period (before and after the division point) by fit-time windows function (Wyss & Habermann, 1988;*

Wyss & Wiemer 2000), the time variation function defines the variation between the rate before and after at local time-scale.

Despite that the migration rate associated with the Mw7.1 Ridgecrest aftershocks rate appears to be slightly higher than that of the Colfiorito sequence, the fluid diffusivity value obtained during the Mw 7.1 postseismic deformation phase (i.e. 275 m^2/s) seems to be quite similar to that observed for the entire Colfiorito sequence, taking into account the anisotropic nature of fluid diffusivity (Antonioli *et al.,* 2005). Such a value of the fluid diffusivity is larger than the 2.32 m^2/s deduced from the poroelastic stress modeling imparted to the Mw 6.4 foreshock (Figure S13; Kariche, 2022) or obtained in the laboratory measurement for the same lithologies. However, it is consistent with estimates of hydraulic diffusivity along Central Italian active faults (Malagnini, 2012; Malagnini *et al.,* 2022), with in-situ measurements at the Long Valley Caldera geothermal field (Roeloffs *et al.,* 2003), and with values deduced from the analysis of induced seismicity due to wastewater injection in Western Oklahoma (Dempsey & Riffault, 2019). Furthermore, using the poromechanical model of Byerlee (1993), I estimate that permeability along the Ridgecrest fault zone increased by up to three orders of magnitude (ranging from 10^{-11} to 10^{-12} m^2) following the Mw 7.1 mainshock. This enhancement in permeability is consistent with the inferred fluid diffusivity of 275 m^2/s and reflects a significant change in fault zone properties during the Mw 7.1 Ridgecrest earthquake.

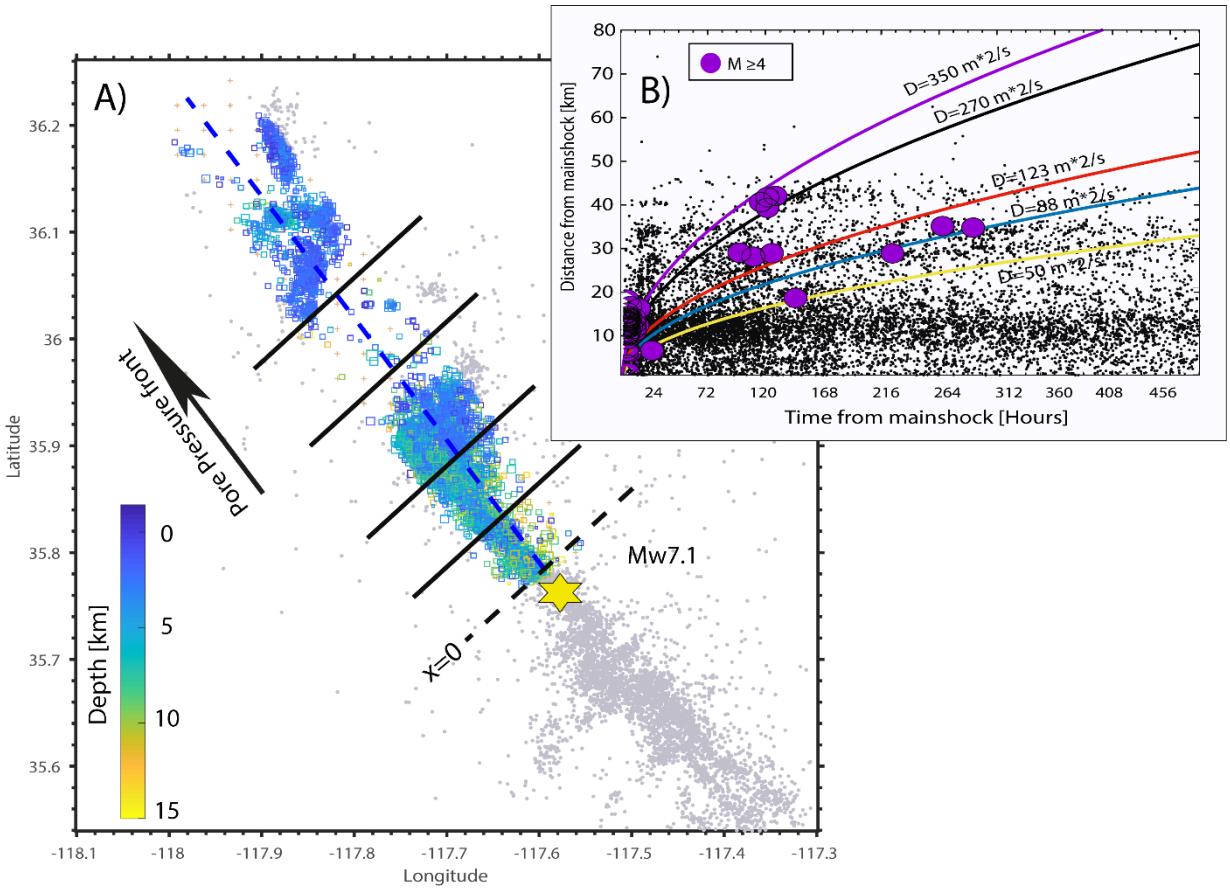

Figure 12: *Spatiotemporal Evolution of Seismicity with M ≥ 2.5 Following the Mw7.1 Mainshock (~20 Days)* ***A)*** *Map showing seismic activity along the northern segment of the Mw7.1 Ridgecrest fault zone, which is used as input data for the pore fluid pressure diffusion modeling. The yellow star marks the epicenter of the Mw7.1 mainshock. Black lines represent the modeled pore pressure fronts.* ***B)*** *Time-distance plot of seismic events occurring in the northern segment of the Mw7.1 Ridgecrest fault zone. Events included in this plot were selected based on their location in the northern area of the Mw7.1 mainshock, as shown in A). The colored parabolic-like envelopes represent a linear diffusion-type approximation (~ √t) of the triggering front. These triggering fronts are calculated using the pressure-diffusion propagation solution in an effective isotropic homogeneous poroelastic medium* (Shapiro, 2015, *Ch.3, Sect.3.3). Fluid diffusivity values are determined for each distance-versus-time (r-t) plot with respect to the distribution of earthquakes with M ≥ 4.*

DISCUSSION AND CONCLUSIONS

The high quality of the Southern California and Central Apennines earthquake catalogs offers us the possibility to study in detail the evolution of seismicity and related fluid migration at different time scales. The evolution of seismicity near Ridgecrest and the Central Apennines reveals that the temporal variation in the b-value is probably due to the stress-fluid redistribution along active faults. The b-value time series modeling shows a gradual decrease in the b-value for all sequences. Based on previous laboratory experiment results on water-saturated specimens (Main *et al.,* 1990; Sammonds *et al*., 1992; Proctor *et al*., 2020), the gradual decrease in the b-value may be interpreted as a dilatancy softening mechanism caused by an increase in pore fluid pressure before each seismic event. The remarkable similarities between the evolution of the b-value following the 2019 Ridgecrest and the 2016 Amatrice-Norcia sequences represented by two b-value minima are probably due to similarities in mechanisms controlling the temporal evolution of foreshock-mainshock sequences. The duration of the first b-value peak scales with the magnitude of the first foreshock while the duration of the second peak (33 hr for Ridgecrest and 4 days for Amatrice-Norcia) appears to be independent of the magnitude of related foreshocks-mainshocks. Based on the coupled b-value–stress intensity laboratory experiments (eg. Sammonds *et al*., 1992), the duration of the second peaks may be interpreted as a short-term poroelastic stress redistribution following a fast slip episode. Also, the temporal evolution of the b-value for the Ridgecrest and the Central Apennines fault zone seems to be in good agreement with the fracture mechanics model of water-saturated specimens as proposed by Main *et al.* (1989) who predict an increase in acoustic emission rate in the dilatancy fluid diffusion phase when the static and dynamic stress drop are not necessarily equal.

The idea that the fluids affect the change in the b-value is not necessarily contradicting the explanation proposed by different authors that the b-value may act as a stress meter (e.g. Goebel

924 *et al*., 2013; Scholz, 2015). The conceptual models proposed here suppose that the decrease in
925 the b-value before foreshock is followed by an acceleration in crack growth and eventually an
926 increase in differential stress over time. The only difference may relate to the modeling of the
927 stress evolution from the period between the foreshock and the mainshock, where the
928 acceleration of the crack front would be expected a decrease in elastic stress. At this time, the
929 decrease in elastic stress is compensated by the increase in pore fluid pressure in time and
930 therefore increases the Coulomb stress change on the receiver faults responsible for the large
931 rupturing process. In this study, the elevated pore-fluid pressure due to the fluid migration in
932 heterogeneous fault zone tends to affect the value of permeability and creates an area with a
933 low-stress drop tendency. Also, the occurrence of the Mw7.1 Ridgecrest right-lateral
934 earthquake is not necessarily associated with the presence of a large deep fluid reservoir. The
935 rapid fluctuation of the b-value just before the Mw7.1 may denote a rapid influx of fluid from
936 surrounding rocks, creating a pore fluid instability on nearby heterogeneous fault ruptures. The
937 temporal evolution of fault permeability and related pore-fluid diffusion appears to be a crucial
938 element in the apprehension of the difference in the time delay between earthquakes in the
939 Central Apennines and the SWL-ECSZ.

940 The interpretation presented in this study, based on the combined temporal evolution of
941 b-values and poromechanical processes, supports the role of complex fluid dynamics in
942 influencing foreshock behavior. Importantly, this perspective does not exclude the accelerating
943 moment release (AMR) hypothesis as a plausible explanation for moderate foreshock activity.
944 In the case of the 2009 L'Aquila sequence, the accelerating strain release (ASR) and pore fluid
945 diffusion (PFD) models likely represent complementary physical processes operating at
946 different spatial and temporal scales. The b-value time series presented here, which accounts
947 for fluid-related effects, is consistent with previous studies suggesting that multiple
948 mechanisms contributed to the preparatory phase of the L'Aquila earthquake. Supporting this

949 dual-process interpretation, Picozzi *et al.* (2022) reported that approximately one week before
950 the mainshock, the rupture initiation phase was characterized by elevated Energy Index (EI)
951 values, indicative of enhanced slip per unit stress. This behavior correlates with a concurrent
952 drop in b-values and lends mechanical support to the model of overpressurized fluid diffusion
953 into the fault zone. As the foreshock sequence progressed, the temporal evolution of dynamic
954 source parameters revealed a transition toward strain-controlled rupture nucleation. These
955 findings support a complex, hybrid preparatory model in which early-stage fluid overpressure
956 facilitates fault weakening and nucleation, while progressive tectonic stress accumulation
957 ultimately drives the Mw 6.3 L'Aquila mainshock.

958 In the same register, Gulia *et al.* (2020) developed a real-time earthquake monitoring
959 system based on a traffic–light classification that uses the temporal change in b-value to
960 constrain whether an ongoing earthquake sequence represents a decaying aftershock phase or
961 precursors to an upcoming large event. Dascher-Cousineau *et al.* (2020) published a paper that
962 points out that the methodology proposed by Gulia *et al*. (2020) gives results in terms of
963 evaluating the risk of a large impending earthquake during the Mw 6.4 Ridgecrest foreshock,
964 this method fails to predict the onset of the Mw 7.1 sequence. Also, Dascher-Cousineau *et al*.
965 (2020) show that for the case of the 2019 Ridgecrest sequence, anomalous earthquake
966 productivity in adjacent regions may affect the background b-values and generate a false alarm.
967 In this study, the b-value time series interpretation taking into account the poroelastic properties
968 of the seismogenic zone shows difficulties to establish a good correlation between the duration
969 of the foreshock activities and the magnitude of the next largest expected earthquake. Despite
970 the fact that the inverse dependency of the b-value and the applied stress appears to be a
971 reasonable interpretation of the b-value drop prior to the Italian and Californian sequences
972 (Gulia & Wiemer, 2019; Gulia *et al*. 2020; Figure S13), the fluctuations of the b-value following
973 the 2019 Ridgecrest and 2016 Amatrice foreshock sequences characterized by a double

974 minimum seem to unfollow the hypothesis that the drop in the b-value before mainshocks is
975 only due to the presence of high-stress levels on receiver main ruptures. This may suggest that
976 the magnitude of the large expected earthquake is controlled by the variations in pore-fluid
977 pressure rather than the maximum differential stress.

978 In the case of immature faults as for the 2019 Ridgecrest earthquake sequence, fluctuations
979 in fluid mass balance can induce significant dilatancy effects. These effects, in turn, impact the
980 evolution of pore-fluid pressure along the fault and could potentially directly influence the
981 dynamic strength of the fault. Mechanically, the pore pressure drop during the dilatancy phase
982 would be recovered at a short time scale by increasing pore-fluid pressure due to the fluid
983 redistribution along the shear zone. If we assume that fault slip is governed by the balance
984 between the frictional strength and the shear stress acting on a fault (Segall & Rice, 1995;
985 Heimisson *et al.*, 2022), the increase in pore-fluid pressure tends to reduce the effective normal
986 stress along the receiver fault. Consequently, this increase in pore fluid pressure can lead to an
987 accelerated slip rate, thereby affecting the size of earthquakes.

988 The physics model of aftershock occurrence as proposed in this paper and based on the
989 dilatancy-diffusion hypothesis validates the assumption that a part of the production of
990 aftershocks is intimately linked to the fluid flow diffusion process. The $1/\sqrt{t}$ rate decay in the
991 aftershock's activity observed in the days following the Mw 6.0 Colfiorito and the Mw 7.1
992 Ridgecrest mainshocks is interpreted as an increase in aftershock productivity due to the pore
993 fluid diffusion along the Colfiorito and Ridgecrest fault zones. The seismicity distribution for
994 extensional earthquakes in Central Apennines shows a seismic migration velocity of 1-3.5
995 km/day during the mainshock-aftershock sequence that indicates a high fluid diffusivity ranging
996 from 60-2000m^2/s (Catalli *et al.,* 2008; Lombardi *et al.,* 2010; Chiaraluce, 2012; Malagnini et
997 al., 2022). Spatiotemporal analysis of the Ridgecrest aftershock sequence reveals that the short-
998 term seismicity migration along the northern part of the Mw7.1 earthquake occurs at a rate of

approximately 4 km/day with an apparent fluid diffusivity ranging from 50-270 m^2/s. This rate is consistent with those observed in Central Apennines, suggesting significant fluid drainage contributing to aftershock productivity.

The kinematic and physical properties of the fault zone may explain the substantial differences in fluid diffusivity before and after the Mw 7.1 Ridgecrest main event. The low fluid diffusivity obtained during the Mw 6.4 foreshock sequence is explained by the poroelastic stress mechanism used in the modeling of fault interactions, which account for stress-fluid interactions. This low diffusivity value suggests that fluid drainage is limited by the anisotropy of the fault zone permeability where the Mw 6.4 conjugated right-lateral rupture acts as a fluid barrier. In this scenario, the poroelastic properties of the seismogenic zone led to elevated pore fluid pressure, affecting the effective normal stress on the delayed Mw 7.1 fault rupture. Thus, the Mw 6.4 foreshock sequence may be seen as a poroelastic undrained-drained preparatory phase that precedes the larger Mw 7.1 event. The significant dilatancy effect during the coseismic phase of the Mw 7.1 earthquake tends to drastically increase fault zone permeability, thereby facilitating fluid drainage. This implies that, during the Mw 7.1-early aftershock period, the Ridgecrest fault zone acts as a "fluid drainage channel". Consequently, the high fluid flow resulting from the change in permeability generates a large pore pressure front that affects the aftershock behavior.

The analysis of the spatiotemporal evolution of seismicity combined with the results of poroelastic stress change as presented in this study testifies that a large portion of aftershocks occurred within fluid-saturated regions largely decoupled from both shallow and deep afterslip patches as identified in geodetic models (Pollitz et al., 2022; He et al., 2022; Yue et al., 2021; Qiu et al., 2020). These afterslip zones are typically associated with rate-strengthening frictional behavior, where deformation is accommodated aseismically through stable sliding. Moreover, near-field GNSS stations located in the northwestern portion of the Mw 7.1 rupture zone

recorded fault-normal displacements consistent with early InSAR observations (Brooks et al., 2020; Wang & Bürgmann, 2020), suggesting that poroelastic rebound, rather than afterslip, dominated the early postseismic deformation. In contrast, the southern Mw 7.1 fault exhibits a distinctly different postseismic signature. Stress change modeling indicates that poroelastic stress changes in this area had a predominantly negative (inhibitive) effect on fault failure, and fluid diffusion processes appear to be absent or negligible. Instead, borehole strainmeters located in this zone reveal a strong and spatially focused afterslip signal (Hirakawa & Barbour, 2020; Hanagan et al., 2024), suggesting that afterslip played a more dominant role.

The spatiotemporal distribution of aftershocks following the 2019 Ridgecrest earthquake is complex (Ross *et al.* 2019; Trugman, 2020). The complex slip distribution and the heterogeneity in fault zone tend to maintain elevated fluid pressure and in fact, increase aftershock productivity. The analysis of seismicity shows that the concentration of seismicity immediately after the Mw 7.1 shut down along the Mw 6.4 conjugated rupture and therefore the aftershock distribution was mainly concentrated along the Mw 7.1 right-lateral fault plane (Toda & Stein, 2020). This observation supports the idea that in general, the fluid migrates linearly at a short-time scale and suppresses the possibility that the fluid flows out of local high-pressure compartments just after the occurrence of the Mw 7.1 mainshock. However, complexity in the slip distribution and geometry of fault rupture may perturb the fluid pressure distribution and give rise to a heterogeneous fluid-flow process at a local scale. At this time, more detailed aftershock modeling procedures (e.g., Yamashita & Tsutsumi, 2018, Sect. 6.3) may be included to give a complete estimation of the complex fluid-flow process. Note that these results are also valid for the Central Apennines sequences.

A more complete 3-D pore-pressure analysis and a careful analysis of the spatiotemporal evolution of stress drop along active faults may mimic the level of effective stress before, during, and after major earthquake sequences. This approach may yield a more accurate

estimation of the evolution of the fluid-flow processes within active fault zones. Based on our results, detailed knowledge of geological structures, substratum permeability, and a robust evaluation of the pore fluid effect with a better constrain of seismicity and strain rate before and during seismic sequences combined with a more complete physics-based and statistical forecast methods appears to be fundamental for the seismic hazard assessment and any decision making.

DATA AVAILABILITY STATEMENTS

The global earthquake catalogs can be downloaded from the Istituto Nazionale Di Geofisica E Vulcanology (INGV) at http://terremoti.ingv.it/en and the U.S. Geological Survey (USGS-NEIC) at https://earthquake.usgs.gov/earthquakes/search/. The earthquake focal mechanisms were obtained through the Global Centroid Moment Tensor solutions available at https://www.globalcmt.org/CMTsearch.html. The Quake Template Matching (QTM) catalog for Southern California, necessary to produce the Ridgecrest time series, was acquired from Ross et al. (2019) in its original form at https://scedc.caltech.edu/data/qtm-catalog.html. The QTM catalog was combined with the higher-resolution Ridgecrest datasets from Shelly (2020), available at https://www.sciencebase.gov/catalog/item/5dd715f3e4b0695797650d18. The Tan et al (2021) catalog used in the b-value time series can be found in the Zenodo dataset repository (https://zenodo.org/records/4662870). The Mw7.1 Ridgecrest source time function can be downloaded from IRIS at https://ds.iris.edu/spud/momenttensor. The Xu et al (2020) Ridgecrest fault slip model was downloaded in its original form from the SRCMOD project (http://equake-rc.info/srcmod/). The converted Matlab format, necessary for performing the stress change modeling, is available through the Zenodo platform at https://zenodo.org/records/10029978. All datasets required to reproduce the b-value time series and stress change modeling in connection with this study are available in Matlab and Coulomb input formats at https://zenodo.org/records/10029978.

ACKNOWLEDGMENTS

The author wishes to express sincere gratitude to M. Meghraoui (ITES, University of Strasbourg) and R. Toussaint (ITES, University of Strasbourg) for insightful discussions on the conceptual framework of stress transfer and poroelastic deformation. Special thanks are extended to Andrew J. Barbour (USGS) and Teruo Yamashita (The University of Tokyo) for their careful review of an earlier version of the manuscript and for their valuable suggestions and comments. The author is equally grateful to the anonymous reviewer for their thorough evaluation and constructive feedback, and to the Editor, Maurizio Ripepe, for his technical support throughout the review process. This research was supported by the Direction of Research at MESRS (Algeria) and the Direction Europe de la Recherche et Coopération Internationale (DERCI-CNRS). Several figures were prepared using the public-domain Generic Mapping Tools (GMT) software (Wessel & Smith, 1998).

DECLARATION OF COMPETING INTEREST

The author confirms that he has no competing financial interests or personal relationships that could have influenced the work reported in this paper.

REFERENCES

Abramowitz, M., & Stegun, I. (1970). Dover. *Handbook of mathematical functions*.

Aki, K. (1965). Maximum likelihood estimate of b in the formula log N= a-bM and its confidence limits. *Bull. Earthq. Res. Inst., Tokyo Univ.*, *43*, 237-239.

Amato, A., Azzara, R., Chiarabba, C., Cimini, G., Cocco, M., Di Bona, M., Margheriti, L., Mazza, S., Mele, F., & Selvaggi, G. (1998). The 1997 Umbria-Marche, Italy, earthquake sequence : A first look at the main shocks and aftershocks. *Geophysical Research Letters*, *25*(15), 2861-2864.

1096 Antoine, S. L., Klinger, Y., Delorme, A., Wang, K., Bürgmann, R., & Gold, R. D. (2021).
1097 Diffuse deformation and surface faulting distribution from submetric image correlation
1098 along the 2019 Ridgecrest, California, ruptures. *Bull. Seismol. Soc. Am.*, *5*, 2275-2302.
1099 Antonioli, A., Piccinini, D., Chiaraluce, L., & Cocco, M. (2005). Fluid flow and seismicity
1100 pattern : Evidence from the 1997 Umbria-Marche (central Italy) seismic sequence.
1101 *Geophysical Research Letters*, *32*(10).
1102 Axen, G. J. (1992). Pore pressure, stress increase, and fault weakening in low-angle normal
1103 faulting. *Journal of Geophysical Research*, *97*(B6), 8979.
1104 https://doi.org/10.1029/92JB00517
1105 Barnhart, W. D., Hayes, G. P., & Gold, R. D. (2019). The July 2019 Ridgecrest, California
1106 Earthquake Sequence : Kinematics of Slip and Stressing in Cross-Fault Ruptures.
1107 *Geophysical Research Letters*, *0*(ja). https://doi.org/10.1029/2019GL084741
1108 Beeler, N., Simpson, R., Hickman, S., & Lockner, D. (2000). Pore fluid pressure, apparent
1109 friction, and Coulomb failure. *Journal of Geophysical Research: Solid Earth*, *105*(B11),
1110 25533-25542.
1111 Berg, E. (1968). Relation between earthquake foreshocks, stress and mainshocks. *Nature*,
1112 *219*(5159), 1141-1143.
1113 Biot, M. A. (1965). *Mechanics of incremental deformations*.
1114 Booker, J. R. (1974). Time dependent strain following faulting of a porous medium. *Journal of*
1115 *Geophysical Research*, *79*(14), 2037-2044.
1116 Bosl, W., & Nur, A. (2002). Aftershocks and pore fluid diffusion following the 1992 Landers
1117 earthquake. *Journal of Geophysical Research: Solid Earth*, *107*(B12), ESE-17.
1118 Brantut, N. (2020). Dilatancy-induced fluid pressure drop during dynamic rupture : Direct
1119 experimental evidence and consequences for earthquake dynamics. *Earth and Planetary*
1120 *Science Letters*, *538*, 116179. https://doi.org/10.1016/j.epsl.2020.116179

Brooks, B. A., Murray, J., Svarc, J., Phillips, E., Turner, R., Murray, M., Ericksen, T., Wang, K., Minson, S., & Burgmann, R. (2020). Rapid geodetic observations of spatiotemporally varying postseismic deformation following the Ridgecrest earthquake sequence : The US Geological Survey response. *Seismological Research Letters*, *91*(4), 2108-2123.

Byerlee, J. D. (1993). Model for episodic flow of high-pressure water in fault zones before earthquakes. *Geology*, *21*(4), 303-306.

Cappa, F., Scuderi, M. M., Collettini, C., Guglielmi, Y., & Avouac, J.-P. (2019). Stabilization of fault slip by fluid injection in the laboratory and in situ. *Science advances*, *5*(3), eaau4065.

Catalli, F., Cocco, M., Console, R., & Chiaraluce, L. (2008). Modeling seismicity rate changes during the 1997 Umbria-Marche sequence (central Italy) through a rate- and state-dependent model. *Journal of Geophysical Research: Solid Earth*, *113*(B11), 2007JB005356. https://doi.org/10.1029/2007JB005356

Chambon, G., & Rudnicki, J. W. (2001). Effects of normal stress variations on frictional stability of a fluid-infiltrated fault. *Journal of Geophysical Research: Solid Earth*, *106*(B6), 11353-11372.

Cheloni, D., De Novellis, V., Albano, M., Antonioli, A., Anzidei, M., Atzori, S., Avallone, A., Bignami, C., Bonano, M., Calcaterra, S., Castaldo, R., Casu, F., Cecere, G., De Luca, C., Devoti, R., Di Bucci, D., Esposito, A., Galvani, A., Gambino, P., … Doglioni, C. (2017). Geodetic model of the 2016 Central Italy earthquake sequence inferred from InSAR and GPS data. *Geophysical Research Letters*, *44*(13), 6778-6787. https://doi.org/10.1002/2017GL073580

Chen, C.-T., Chan, Y.-C., Beyssac, O., Lu, C.-Y., Chen, Y.-G., Malavieille, J., Kidder, S. B., & Sun, H.-C. (2019). Thermal History of the Northern Taiwanese Slate Belt and

1146 Implications for Wedge Growth During the Neogene Arc-Continent Collision.
1147 *Tectonics*, *38*(9), 3335-3350. https://doi.org/10.1029/2019TC005604
1148 Chiarabba, C., Buttinelli, M., Cattaneo, M., & De Gori, P. (2020). Large earthquakes driven by
1149 fluid overpressure : The Apennines normal faulting system case. *Tectonics*, *39*(4),
1150 e2019TC006014.
1151 Chiaraluce, L., Ellsworth, W., Chiarabba, C., & Cocco, M. (2003). Imaging the complexity of
1152 an active normal fault system : The 1997 Colfiorito (central Italy) case study. *Journal*
1153 *of Geophysical Research: Solid Earth*, *108*(B6).
1154 Chiodini, G., Cardellini, C., Amato, A., Boschi, E., Caliro, S., Frondini, F., & Ventura, G.
1155 (2004). Carbon dioxide Earth degassing and seismogenesis in central and southern Italy.
1156 *Geophysical Research Letters*, *31*(7).
1157 Cocco, M., & Rice, J. R. (2002). Pore pressure and poroelasticity effects in Coulomb stress
1158 analysis of earthquake interactions. *Journal of Geophysical Research: Solid Earth*,
1159 *107*(B2), ESE-2.
1160 Combs, J. (1980). Heat flow in the Coso Geothermal Area, Inyo County, California. *Journal of*
1161 *Geophysical Research*, *85*(B5), 2411. https://doi.org/10.1029/JB085iB05p02411
1162 Dascher-Cousineau, K., Lay, T., & Brodsky, E. E. (2020). Two foreshock sequences post Gulia
1163 and Wiemer (2019). *Seismological Society of America*, *91*(5), 2843-2850.
1164 De Barros, L., Cappa, F., Deschamps, A., & Dublanchet, P. (2020). Imbricated aseismic slip
1165 and fluid diffusion drive a seismic swarm in the Corinth Gulf, Greece. *Geophysical*
1166 *Research Letters*, *47*(9), e2020GL087142.
1167 Dempsey, D., & Riffault, J. (2019). Response of induced seismicity to injection rate reduction :
1168 Models of delay, decay, quiescence, recovery, and Oklahoma. *Water Resources*
1169 *Research*, *55*(1), 656-681.

1170 Deschamps, A., Courboulex, F., Gaffet, S., Lomax, A., Virieux, J., Amato, A., Azzara, A.,
1171 Castello, B., Chiarabba, C., & Cimini, G. (2000). Spatio-temporal distribution of
1172 seismic activity during the Umbria-Marche crisis, 1997. *Journal of Seismology*, *4*(4),
1173 377-386.
1174 Ekström, G., Morelli, A., Boschi, E., & Dziewonski, A. M. (1998). Moment tensor analysis of
1175 the central Italy earthquake sequence of September–October 1997. *Geophysical*
1176 *Research Letters*, *25*(11), 1971-1974.
1177 Enescu, B., Mori, J., & Miyazawa, M. (2007). Quantifying early aftershock activity of the 2004
1178 mid-Niigata Prefecture earthquake (Mw6.6). *Journal of Geophysical Research: Solid*
1179 *Earth*, *112*(B4). https://doi.org/10.1029/2006JB004629
1180 Fielding, E. J., Liu, Z., Stephenson, O. L., Zhong, M., Liang, C., Moore, A., Yun, S., & Simons,
1181 M. (2020). Surface Deformation Related to the 2019 M w 7.1 and 6.4 Ridgecrest
1182 Earthquakes in California from GPS, SAR Interferometry, and SAR Pixel Offsets.
1183 *Seismological Research Letters*.
1184 Gardner, J., & Knopoff, L. (1974). Is the sequence of earthquakes in Southern California, with
1185 aftershocks removed, Poissonian? *Bulletin of the seismological society of America*,
1186 *64*(5), 1363-1367.
1187 Gasperini, P., Lolli, B., & Vannucci, G. (2013). Empirical calibration of local magnitude data
1188 sets versus moment magnitude in Italy. *Bulletin of the Seismological Society of America*,
1189 *103*(4), 2227-2246.
1190 Goebel, T. H. W., Schorlemmer, D., Becker, T. W., Dresen, G., & Sammis, C. G. (2013).
1191 Acoustic emissions document stress changes over many seismic cycles in stick-slip
1192 experiments. *Geophysical Research Letters*, *40*(10), 2049-2054.
1193 https://doi.org/10.1002/grl.50507

1194 Gulia, L., Tormann, T., Wiemer, S., Herrmann, M., & Seif, S. (2016). Short-term probabilistic
1195 earthquake risk assessment considering time-dependent b values. *Geophysical Research*
1196 *Letters*, *43*(3), 1100-1108. https://doi.org/10.1002/2015GL066686
1197 Gulia, L., & Wiemer, S. (2019). Real-time discrimination of earthquake foreshocks and
1198 aftershocks. *Nature*, *574*(7777), 193-199.
1199 Gulia, L., Wiemer, S., & Vannucci, G. (2020). Pseudoprospective Evaluation of the Foreshock
1200 Traffic-Light System in Ridgecrest and Implications for Aftershock Hazard
1201 Assessment. *Seismological Society of America*, *91*(5), 2828-2842.
1202 Guo, Z., & Ogata, Y. (1997). Statistical relations between the parameters of aftershocks in time,
1203 space, and magnitude. *Journal of Geophysical Research: Solid Earth*, *102*(B2),
1204 2857-2873.
1205 Gutenberg, G., & Richter, C. (1950). Seismicity of the earth and associated phenomena,
1206 Howard Tatel. *JGR*, *55*, 97.
1207 Hanagan, C., Bennett, R. A., Barbour, A., & Hughes, A. N. (2024). Afterslip and Creep in the
1208 Rate-Dependent Framework : Joint Inversion of Borehole Strain and GNSS
1209 Displacements for the Mw 7.1 Ridgecrest Earthquake. *Journal of Geophysical*
1210 *Research: Solid Earth*, *129*(10), e2024JB028908.
1211 https://doi.org/10.1029/2024JB028908
1212 Hauksson, E., Hutton, K., Kanamori, H., Jones, L., Mori, J., Hough, S., & Roquemore, G.
1213 (1995). Preliminary Report on the 1995 Ridgecrest Earthquake Sequence in Eastern
1214 California. *Seismological Research Letters*, *66*(6), 54-60.
1215 https://doi.org/10.1785/gssrl.66.6.54
1216 He, K., Xu, C., & Wen, Y. (2022). Coseismic and early post-seismic deformations due to the
1217 2019 earthquake sequence in Ridgecrest, California. *Geophysical Journal International*,
1218 *230*(2), 957-975. https://doi.org/10.1093/gji/ggac103

1219 Heimisson, E. R., Liu, S., Lapusta, N., & Rudnicki, J. (2022). A Spectral Boundary-Integral
1220 Method for Faults and Fractures in a Poroelastic Solid : Simulations of a Rate-and-State
1221 Fault With Dilatancy, Compaction, and Fluid Injection. *Journal of Geophysical*
1222 *Research: Solid Earth*, *127*(9), e2022JB024185.
1223 Hickman, S., Sibson, R., & Bruhn, R. (1995). Introduction to special section : Mechanical
1224 involvement of fluids in faulting. *Journal of Geophysical Research: Solid Earth*,
1225 *100*(B7), 12831-12840.
1226 Hirakawa, E., & Barbour, A. J. (2020). Kinematic Rupture and 3D Wave Propagation
1227 Simulations of the 2019 Mw 7.1 Ridgecrest, California, Earthquake. *Bulletin of the*
1228 *Seismological Society of America*, *110*(4), 1644-1659.
1229 https://doi.org/10.1785/0120200031
1230 Hudnut, K. W., Seeber, L., & Pacheco, J. (1989). Cross-fault triggering in the November 1987
1231 Superstition Hills earthquake sequence, southern California. *Geophysical Research*
1232 *Letters*, *16*(2), 199-202.
1233 Kariche, J. (2022). The 2020 Monte Cristo (Nevada) Earthquake Sequence : Stress Transfer in
1234 the Context of Conjugate Strike-Slip Faults. *Tectonics*, *41*(3), e2020TC006506.
1235 Kariche, J., Meghraoui, M., Timoulali, Y., Cetin, E., & Toussaint, R. (2018). The Al Hoceima
1236 earthquake sequence of 1994, 2004 and 2016 : Stress transfer and poroelasticity in the
1237 Rif and Alboran Sea region. *Geophysical Journal International*, *212*(1), 42-53.
1238 https://doi.org/10.1093/gji/ggx385
1239 Khoshmanesh, M., & Shirzaei, M. (2018). Episodic creep events on the San Andreas Fault
1240 caused by pore pressure variations. *Nature geoscience*, *11*(8), 610.
1241 Kirkpatrick, J., Shipton, Z., Evans, J. P., Micklethwaite, S., Lim, S., & McKillop, P. (2008).
1242 Strike-slip fault terminations at seismogenic depths : The structure and kinematics of

1243 the Glacier Lakes fault, Sierra Nevada United States. *Journal of Geophysical Research: Solid Earth*, *113*(B4).
1245 Lombardi, A. M., Cocco, M., & Marzocchi, W. (2010). On the Increase of Background Seismicity Rate during the 1997-1998 Umbria-Marche, Central Italy, Sequence : Apparent Variation or Fluid-Driven Triggering? *Bulletin of the Seismological Society of America*, *100*(3), 1138-1152. https://doi.org/10.1785/0120090077
1249 Main, I. G., Meredith, P. G., & Jones, C. (1989). A reinterpretation of the precursory seismic b-value anomaly from fracture mechanics. *Geophysical Journal International*, *96*(1), 131-138.
1252 Main, I. G., Meredith, P. G., Sammonds, P. R., & Jones, C. (1990). Influence of fractal flaw distributions on rock deformation in the brittle field. *Geological Society, London, Special Publications*, *54*(1), 81-96.
1255 Malagnini, L., Lucente, F. P., De Gori, P., Akinci, A., & Munafo', I. (2012). Control of pore fluid pressure diffusion on fault failure mode : Insights from the 2009 L'Aquila seismic sequence. *Journal of Geophysical Research: Solid Earth*, *117*(B5).
1258 Malagnini, L., Parsons, T., Munafò, I., Mancini, S., Segou, M., & Geist, E. L. (2022). Crustal permeability changes inferred from seismic attenuation : Impacts on multi-mainshock sequences. *Frontiers in Earth Science*, *10*, 963689. https://doi.org/10.3389/feart.2022.963689
1262 Miller, S. A. (2020). Aftershocks are fluid-driven and decay rates controlled by permeability dynamics. *Nature communications*, *11*(1), 1-11.
1264 Monastero, F. C., Walker, J. D., Katzenstein, A. M., Sabin, A. E., Glazner, A., & Bartley, J. (2002). Neogene evolution of the Indian Wells Valley, east-central California. *Geologic evolution of the Mojave Desert and southwestern Basin and Range: Geological Society of America Memoir*, *195*, 199-228.

1268 Moro, M., Saroli, M., Stramondo, S., Bignami, C., Albano, M., Falcucci, E., Gori, S., Doglioni,
1269 C., Polcari, M., & Tallini, M. (2017). New insights into earthquake precursors from
1270 InSAR. *Scientific reports*, *7*(1), 12035.
1271 Nanjo, K., Hirata, N., Obara, K., & Kasahara, K. (2012). Decade-scale decrease inb value prior
1272 to the M9-class 2011 Tohoku and 2004 Sumatra quakes. *Geophysical Research Letters*,
1273 *39*(20).
1274 Nespoli, M., Belardinelli, M. E., Gualandi, A., Serpelloni, E., & Bonafede, M. (2018).
1275 Poroelasticity and Fluid Flow Modeling for the 2012 Emilia-Romagna Earthquakes :
1276 Hints from GPS and InSAR Data. *Geofluids*, *2018*.
1277 Nur, A., & Booker, J. R. (1972). Aftershocks caused by pore fluid flow? *Science*, *175*(4024),
1278 885-887.
1279 Picozzi, M., Spallarossa, D., Iaccarino, A. G., & Bindi, D. (2022). Temporal Evolution of
1280 Radiated Energy to Seismic Moment Scaling During the Preparatory Phase of the Mw
1281 6.1, 2009 L'Aquila Earthquake (Italy). *Geophysical Research Letters*, *49*(8),
1282 e2021GL097382. https://doi.org/10.1029/2021GL097382
1283 Pino, N. A., Convertito, V., & Madariaga, R. (2019). Clock advance and magnitude limitation
1284 through fault interaction : The case of the 2016 central Italy earthquake sequence.
1285 *Scientific reports*, *9*(1), 5005.
1286 Pio Lucente, F., De Gori, P., Margheriti, L., Piccinini, D., Di Bona, M., Chiarabba, C., & Piana
1287 Agostinetti, N. (2010). Temporal variation of seismic velocity and anisotropy before the
1288 2009 MW 6.3 L'Aquila earthquake, Italy. *Geology*, *38*(11), 1015-1018.
1289 Pollitz, F. F., Wicks, C. W., Svarc, J. L., Phillips, E., Brooks, B. A., Murray, M. H., & Turner,
1290 R. C. (2022). Postseismic relaxation following the 2019 Ridgecrest, California,
1291 earthquake sequence. *Bulletin of the Seismological Society of America*, *112*(2), 734-749.

1292 Proctor, B., Lockner, D., Kilgore, B., Mitchell, T., & Beeler, N. (2020). Direct evidence for
1293 fluid pressure, dilatancy, and compaction affecting slip in isolated faults. *Geophysical*
1294 *Research Letters*, *47*(16), e2019GL086767.
1295 Qiu, Q., Barbot, S., Wang, T., & Wei, S. (2020). Slip complementarity and triggering between
1296 the foreshock, mainshock, and afterslip of the 2019 Ridgecrest rupture sequence.
1297 *Bulletin of the Seismological Society of America*, *110*(4), 1701-1715.
1298 Reasenberg, P. A., & Simpson, R. W. (1992). Response of regional seismicity to the static stress
1299 change produced by the Loma Prieta earthquake. *Science*, *255*(5052), 1687-1690.
1300 Rice, J. R. (1992). Chapter 20 Fault Stress States, Pore Pressure Distributions, and the
1301 Weakness of the San Andreas Fault. In *International Geophysics* (Vol. 51, p. 475-503).
1302 Elsevier. https://doi.org/10.1016/S0074-6142(08)62835-1
1303 Rice, J. R., & Cleary, M. P. (1976). Some basic stress diffusion solutions for fluid-saturated
1304 elastic porous media with compressible constituents. *Reviews of Geophysics*, *14*(2),
1305 227-241.
1306 Rikitake, T. (1972). Earthquake prediction studies in Japan. *Geophysical surveys*, *1*(1), 4-26.
1307 Ripepe, M., Piccinini, D., & Chiaraluce, L. (2000). Foreshock sequence of september 26th,
1308 1997 Umbria-Marche earthquakes. *Journal of Seismology*, *4*, 387-399.
1309 Roeloffs, E., Sneed, M., Galloway, D. L., Sorey, M. L., Farrar, C. D., Howle, J. F., & Hughes,
1310 J. (2003). Water-level changes induced by local and distant earthquakes at Long Valley
1311 caldera, California. *Journal of Volcanology and Geothermal Research*, *127*(3-4),
1312 269-303.
1313 Ross, Z. E., Trugman, D. T., Hauksson, E., & Shearer, P. M. (2019). Searching for hidden
1314 earthquakes in Southern California. *Science*, *364*(6442), 767-771.

1315 Ruhl, C., Abercrombie, R., Smith, K., & Zaliapin, I. (2016). Complex spatiotemporal evolution
1316 of the 2008 Mw 4.9 Mogul earthquake swarm (Reno, Nevada) : Interplay of fluid and
1317 faulting. *Journal of Geophysical Research: Solid Earth*, *121*(11), 8196-8216.
1318 Sammonds, P., Meredith, P., & Main, I. (1992). Role of pore fluids in the generation of seismic
1319 precursors to shear fracture. *Nature*, *359*(6392), 228-230.
1320 Scholz, C. H. (1968). The frequency-magnitude relation of microfracturing in rock and its
1321 relation to earthquakes. *Bulletin of the Seismological Society of America*, *58*(1),
1322 399-415. https://doi.org/10.1785/BSSA0580010399
1323 Scholz, C. H. (2015). On the stress dependence of the earthquake b value. *Geophysical*
1324 *Research Letters*, *42*(5), 1399-1402.
1325 Scholz, C. H. (2019). *The mechanics of earthquakes and faulting*. Cambridge university press.
1326 Segall, P. (2010). *Earthquake and volcano deformation*. Princeton University Press.
1327 Segall, P., & Rice, J. R. (1995). Dilatancy, compaction, and slip instability of a fluid-infiltrated
1328 fault. *Journal of Geophysical Research: Solid Earth*, *100*(B11), 22155-22171.
1329 Serpelloni, E., Anzidei, M., Baldi, P., Casula, G., & Galvani, A. (2005). Crustal velocity and
1330 strain-rate fields in Italy and surrounding regions : New results from the analysis of
1331 permanent and non-permanent GPS networks. *Geophysical Journal International*,
1332 *161*(3), 861-880.
1333 Shapiro, S. A. (2015). *Fluid-induced seismicity*. Cambridge University Press.
1334 Shi, Y., & Bolt, B. A. (1982). The standard error of the magnitude-frequency b value. *Bulletin*
1335 *of the Seismological Society of America*, *72*(5), 1677-1687.
1336 Sibson, R. H. (2000). Fluid involvement in normal faulting. *Journal of Geodynamics*, *29*(3-5),
1337 469-499.
1338 Smith, W. D. (1981). The b-value as an earthquake precursor. *Nature*, *289*(5794), 136-139.

1339 Soldati, G., Zaccarelli, L., & Faenza, L. (2019). Spatio-temporal seismic velocity variations
1340 associated to the 2016–2017 central Italy seismic sequence from noise cross-correlation.
1341 *Geophysical Journal International*, *219*(3), 2165-2173.
1342 Stramondo, S., Tesauro, M., Briole, P., Sansosti, E., Salvi, S., Lanari, R., Anzidei, M., Baldi,
1343 P., Fornaro, G., & Avallone, A. (1999). The September 26, 1997 Colfiorito, Italy,
1344 earthquakes : Modeled coseismic surface displacement from SAR interferometry and
1345 GPS. *Geophysical research letters*, *26*(7), 883-886.
1346 Tan, Y. J., Waldhauser, F., Ellsworth, W. L., Zhang, M., Zhu, W., Michele, M., Chiaraluce, L.,
1347 Beroza, G. C., & Segou, M. (2021). Machine-learning-based high-resolution earthquake
1348 catalog reveals how complex fault structures were activated during the 2016–2017
1349 Central Italy sequence. *The Seismic Record*, *1*(1), 11-19.
1350 Toda, S., & Stein, R. S. (2020). Long-and short-term stress interaction of the 2019 Ridgecrest
1351 sequence and Coulomb-based earthquake forecasts. *Bulletin of the Seismological*
1352 *Society of America*, *110*(4), 1765-1780.
1353 Tong, P., Yao, J., Liu, Q., Li, T., Wang, K., Liu, S., Cheng, Y., & Wu, S. (2021). Crustal rotation
1354 and fluids : Factors for the 2019 Ridgecrest earthquake sequence? *Geophysical*
1355 *Research Letters*, *48*(3), e2020GL090853.
1356 Tormann, T., Wiemer, S., Metzger, S., Michael, A., & Hardebeck, J. L. (2013). Size distribution
1357 of Parkfield's microearthquakes reflects changes in surface creep rate. *Geophysical*
1358 *Journal International*, *193*(3), 1474-1478. https://doi.org/10.1093/gji/ggt093
1359 Tung, S., & Masterlark, T. (2018). Delayed poroelastic triggering of the 2016 October Visso
1360 earthquake by the August Amatrice earthquake, Italy. *Geophysical Research Letters*,
1361 *45*(5), 2221-2229.
1362 Utsu, T., & Ogata, Y. (1995). The centenary of the Omori formula for a decay law of aftershock
1363 activity. *Journal of Physics of the Earth*, *43*(1), 1-33.

1364 Wang, K., & Bürgmann, R. (2020). Co- and Early Postseismic Deformation Due to the 2019
1365 Ridgecrest Earthquake Sequence Constrained by Sentinel-1 and COSMO-SkyMed SAR
1366 Data. *Seismological Research Letters*. https://doi.org/10.1785/0220190299
1367 Wang, K., Dreger, D. S., Tinti, E., Bürgmann, R., & Taira, T. (2020). Rupture process of the
1368 2019 Ridgecrest, California M w 6.4 foreshock and M w 7.1 earthquake constrained by
1369 seismic and geodetic data. *Bulletin of the Seismological Society of America*, *110*(4),
1370 1603-1626.
1371 Wiemer, S. (2001). A software package to analyze seismicity : ZMAP. *Seismological Research*
1372 *Letters*, *72*(3), 373-382.
1373 Wiemer, S., & Wyss, M. (2000). Minimum magnitude of completeness in earthquake catalogs :
1374 Examples from Alaska, the western United States, and Japan. *Bulletin of the*
1375 *Seismological Society of America*, *90*(4), 859-869.
1376 Woessner, J., & Wiemer, S. (2005). Assessing the quality of earthquake catalogues : Estimating
1377 the magnitude of completeness and its uncertainty. *Bulletin of the Seismological Society*
1378 *of America*, *95*(2), 684-698.
1379 Wyss, M., & Habermann, R. E. (1988). Precursory seismic quiescence. *Pure and Applied*
1380 *Geophysics*, *126*(2), 319-332.
1381 Wyss, M., & McNutt, S. R. (1998). Temporal and three-dimensional spatial analyses of the
1382 frequency–magnitude distribution near Long Valley Caldera, California. *Geophysical*
1383 *Journal International*, *134*(2), 409-421.
1384 Wyss, M., & Wiemer, S. (2000). Change in the probability for earthquakes in southern
1385 California due to the Landers magnitude 7.3 earthquake. *Science*, *290*(5495),
1386 1334-1338.

Xu, X., Sandwell, D. T., & Smith-Konter, B. (2020). Coseismic Displacements and Surface Fractures from Sentinel-1 InSAR : 2019 Ridgecrest Earthquakes. *Seismological Research Letters*. https://doi.org/10.1785/0220190275

Yamashita, T., & Tsutsumi, A. (2018a). *Involvement of Fluids in Earthquake Ruptures*. Springer Japan. https://doi.org/10.1007/978-4-431-56562-8

Yehya, A., Yang, Z., & Rice, J. R. (2018). Effect of fault architecture and permeability evolution on response to fluid injection. *Journal of Geophysical Research: Solid Earth*, *123*(11), 9982-9997.

Yue, H., Sun, J., Wang, M., Shen, Z., Li, M., Xue, L., Lu, W., Zhou, Y., Ren, C., & Lay, T. (2021). The 2019 Ridgecrest, California earthquake sequence : Evolution of seismic and aseismic slip on an orthogonal fault system. *Earth and Planetary Science Letters*, *570*, 117066.